

LA-UR-14-29056

Approved for public release; distribution is unlimited.

Title: Seismicity of the Western Greenland Ice Sheet: Surface Fracture in the Vicinity of Active Moulins

Author(s): Carmichael, Joshua Daniel
Joughin, Ian R.
Behn, Mark D.
Das, Sarah B.
King, Matt A.
Stevens, Laura
Lizarralde, Daniel

Intended for: Journal of Geophysical Research, Earth Surface

Issued: 2014-11-21

Disclaimer:

Los Alamos National Laboratory, an affirmative action/equal opportunity employer, is operated by the Los Alamos National Security, LLC for the National Nuclear Security Administration of the U.S. Department of Energy under contract DE-AC52-06NA25396. By approving this article, the publisher recognizes that the U.S. Government retains nonexclusive, royalty-free license to publish or reproduce the published form of this contribution, or to allow others to do so, for U.S. Government purposes. Los Alamos National Laboratory requests that the publisher identify this article as work performed under the auspices of the U.S. Department of Energy. Los Alamos National Laboratory strongly supports academic freedom and a researcher's right to publish; as an institution, however, the Laboratory does not endorse the viewpoint of a publication or guarantee its technical correctness.

Title

Seismicity of the Western Greenland Ice Sheet: Surface Fracture in the Vicinity of Active Moulins

Authors

Joshua D Carmichael¹, Ian Joughin, Mark D. Behn, Sarah Das, Matt A. King², Laura Stevens, Dan Lizarralde

Abstract

We analyzed geophone and GPS measurements collected from the ablation zone of the western Greenland Ice Sheet during a ~35 day period of the 2011 melt season to study changes in ice deformation before, during and after a supraglacial lake drainage event. During rapid lake drainage, ice flow speeds increased to ~400% of winter values, and icequake activity transiently peaked. At times > 7 days after drainage, this seismicity developed a diurnal and longer period (~10-15 day) variable signal, while coincident ice speeds fell to ~150% of winter values and showed nightly peaks in spatial variability. Approximately 95% of all detectable seismicity in the lake basin and its immediate vicinity was triggered by fracture propagation within near-surface ice (< 330 m deep) that generated Rayleigh waves. Icequakes occurring before and during drainage frequently co-located with the down flow (west) end of the primary hydrofracture through which the lake drained, but shifted farther west and outside the lake basin after the drainage. We interpret these results to reveal vertical hydrofracture opening and local uplift during the drainage, followed by enhanced seismicity and ice flow on the down-stream side of the lake basin. This down-stream region collocates InSAR-measured speedup in previous years, and could reflect the migration path of the melt water supplied to the bed by the lake. The diurnal seismic signal may be associated with nightly reductions in surface melt input that increase effective basal pressure and traction, thereby promoting elevated strain in the surficial ice.

1. Introduction

Supraglacial lakes on the western margin of the Greenland Ice Sheet often drain by hydrofracture, thereby establishing pathways (moulins) for surface meltwater to reach the ice-bed interface and influence basal motion [Das et al., 2008, Joughin et al., 2013; Krawczynski et al., 2009; Selmes et al., 2009; Doyle et al., 2013; Tedesco et al., 2013]. Evidence accumulated to

¹ Now at Earth and Environmental Sciences Division, Los Alamos National Laboratory, Los Alamos NM, USA

² School of Civil Engineering and Geosciences, Newcastle University, Newcastle upon Tyne NE1 7RU, UK
School of Geography and Environmental Studies, University of Tasmania, Hobart 7001, Australia

date suggests that subglacial hydrology is qualitatively similar to that of mountain glaciers where sliding is driven by changes in basal water storage and pressure [e.g., Bartholomew et al., 2011; Shepherd et al., 2009]. Most documented fast (hour-scale) lake-drainage events on the ice sheet occur during early-to-mid summer, often between days of year (DOY) 180 and 210 [Selmes et al., 2011]. Earlier or farther inland moulin formation via lake-drainage brought on by a warmer climate could increase meltwater forcing of less well developed, spring drainage systems [Howat et al., 2013; Liang et al., 2012]. The appearance of such surface-to-bed hydrological connections earlier in the season could therefore trigger a sustained speedup through prolonged basal decoupling, or alternatively, it could reduce speedup by accelerating development of an efficient drainage network [Sundal et al. 2011; Schoof, 2010]. It is therefore important to determine when and where these connections appear on the ice sheet. Often, such pathways form during brittle deformation events that accompany hydrofracture or extensional ice flow (e.g. crevassing), and thereby release seismic radiation (icequakes). Additionally, melt delivered to the bed by these pathways may induce basal icequakes through shearing motion that accompanies sliding. This suggests that the creation and response to hydrological connections in the lake-forming region of the Greenland Ice Sheet can be identified from icequakes to determine the extent to which seismicity reflects seasonal variation in ice flow.

In this paper, we present seismic and geophysical observations collected over the 2011 melt season near a supraglacial lake southeast of Jakobshavn-Isbrae that observations show has drained each summer since 2006 [Das et al., 2008, Das et al. 2011]. Our analyses and interpretation focus on Rayleigh-waveforms generated by shallow ice fractures. In contrast to most previous work, we include several weeks following the lake drainage into these analyses to study the ice-sheet's response to melt input following the creation of the associated moulin. These are therefore among the first seismic observations obtained from Greenland's Ice Sheet that provide continuous data before, during, and > 7 days after a supraglacial lake drainage.

Background

Ice sheet response to meltwater forcing is often monitored using GPS [e.g., Das et al., 2008; Hoffman et al., 2011] or other remote sensing methods that measure ice deformation over time using records of displacement [e.g., Joughin et al. 2008; Joughin et al. 2013; Palmer et al., 2011].

Seismic methods can also be used to observe the effects of melt-triggered ice deformation by detecting and measuring elastic energy released by processes such as hydrofracturing and basal sliding. Some recent ground-based experiments in western Greenland, where supraglacial lakes are prevalent in summer, have therefore also included seismic networks [Das et al., 2008; Doyle et al., 2013; Jones et al., 2013; Roosli et al. 2014]. The earlier of these experiments demonstrated that elevated seismicity accompanied hydrofracture of ice during lake drainage [Das et al., 2008] and tectonic faulting of the ice-sheet column during subsequent hydraulic jacking [Doyle et al., 2013]. In these cases, additional icequake interpretation was limited by inadequate station coverage or a capability to associate waveforms on distinct geophones. Later work identified icequakes triggered by crevassing and moulin resonance under water input using a dense network of surface and borehole seismometers deployed in the ablation zone [Roosli et al, 2014]. Similar experiments that involve alpine and polar glaciers also have used seismic network data to detect and locate sources of icequakes triggered by meltwater [Canassy et al., 2012; Carmichael et al., 2012; Mikesell et al., 2012; Stuart et al. 2005; Walter et al., 2008]. Some of these icequakes have been associated with basal stick-slip [Allstadt and Malone, 2014; Thelen et al., 2013] or basal fracturing during subglacial cavity collapse [Walter et al., 2013]. Other icequakes appear to be associated with shallow processes like brittle deformation of near-surface ice where high tensile stresses develop during meltwater-activated basal sliding [Pomeroy et al., 2013; Roux et al., 2010]. On the Greenland Ice Sheet, it remains unclear which among these processes produce icequake activity, since few experiments have so far been capable of distinguishing surficial from deeper seismicity [e.g., Roosli et al. 2014]. In particular, the extent to which ice sliding over the bed produces basal seismicity remains unknown. Therefore, it is important to establish (1) when and where icequakes are triggered during a melt season in moulin-forming regions of the ice sheet, and (2) whether icequakes represent an indicator of ice-sheet response to hydrological or other forcing, through changes in timing, location or magnitude following drainage.

2. Study Region and Instrumentation

The field location, illustrated in Figure 1, was established in 2006 to study the effects of supraglacial lake drainage on ice deformation and regional flow [Das et al., 2008; Joughin et al., 2008]. Since 2006, geophones, temperature loggers, and GPS receivers have been redeployed

each summer in various configurations around the lake basin. Ablation rates at this elevation (~1050m) are $\sim 2 \text{ m a}^{-1}$ and ice thickness is $\sim 980 \text{ m}$. Stresses in the lake basin are generally compressive due to flow-convergence over a bedrock depression, and become tensile west and northwest of the lake shoreline where the ice thins by a few hundred meters as it flows over a subglacial ridge (Figure 1). Ice flows west-northwest ($\sim 280^\circ$), with mean annual flow rates of $\sim 80 \text{ m a}^{-1}$ ($\sim 22 \text{ cm d}^{-1}$).

In mid-June 2011, the lake perimeter was instrumented with 6 PASSCAL-supplied geophones, 18 UNAVCO-supplied GPS receivers, and an air-temperature logger. Each geophone site was co-located with a GPS station and included a 3-component, 4.5-Hz, L-28 geophone, and a Quanterra Q330 digitizer sampling at 200Hz, logging to a hard drive. All geophones were mounted on identical pole-platform assemblies, which were installed in $\sim 2\text{-m}$ deep ice holes that were back-filled with ice chips. One of these sites, NLBS, is a semi-permanent “base station” that has collected GPS and seismic data near the field camp since 2006 and 2007, respectively. Each GPS site consisted of a Trimble NetRS or NetR9 unit sampling at 1-second intervals. Both the GPS and geophone data were recovered in June 2012. Here, we focus primarily on analysis of the seismic data.

3. Methods

The lake in Figure 1 drained on DOY 169 (June 18, 2011) while the instruments were still being installed, so that only a partially-deployed network (Figure 2) was logging data during the event. Within ~ 12 hours after drainage, we conducted an aerial survey by helicopter over the lake basin to document surface expressions of hydrofracture, including moulin and fracture locations. From these surveys, we determined that the hydrofracture event that occurred during drainage opened a crack at least several hundred meters long and appeared to initiate near a moulin that formed during the previous summer. This crack opened along a remnant high-angle hydrofracture-formed scarp at the lake bottom that was associated with prior drainages described elsewhere [Das et al., 2008].

Our analyses in the following subsections includes the data preceding, during, and several weeks following this lake drainage. In Section 3.1, we describe robust detection statistics used to

quantify icequake emission rates and temporal trends in seismic activity. In Section 3.2, we locate a subset of these icequakes using a novel beamforming-method that also provides estimates of seismic attenuation factors. We further use these locations in Section 3.3 to compute seismic magnitudes, hypocentral deformation volumes, and independent, secondary estimates for attenuation factors. In Section 3.4, we measure relative changes in these icequake magnitudes over time by implementing multi-channel cross-correlation methods. Finally, we process the GPS data in Section 3.5 to compare time series of ice surface uplift and speed with seismicity.

3.1 Icequake Timing and Statistics

We first identified individual icequakes by processing data from the vertical-channel of each geophone using a noise-adaptive, digital power detector. This detector computes a data statistic at each point in a geophone data stream by dividing an estimate of the sample variance within a leading data window by an estimate of the sample variance within a longer, following window i.e., the STA/LTA [Blandford, 1974]. To account for statistically correlated background noise, we computed robust estimates for the degree-of-freedom parameters of the data statistic's F -distribution within each detection window [Carmichael, 2013]. These updated parameters enabled us to dynamically adjust the detector's event declaration threshold within each window and maintain a constant, acceptably low false-detection probability. We set this probability to 10^{-6} using the Neyman-Pearson decision rule [Kay, 1998; Chapter 7], so that waveforms with an SNR of ~ 10 dB had a 95% probability of being detected on a single geophone in average noise conditions. Waveforms then detected on different geophones within a time interval less than the expected transit time of a shear wave across the network were identified as the same icequake (i.e., we performed waveform association). From these detections, we counted events that were large enough to be associated on three or more geophones, and binned this count each hour to measure icequake seismicity. To quantify our confidence in this estimate, we identified time-windows where the predicted null (signal-absent) F -distribution for the STA/LTA statistic matched its histogram with $\leq 20\%$ error. These signals provided our best hourly estimate of the seismicity as well as a measure of confidence in our estimates.

3.2 Hypocentral Distributions and Waveform Attenuation

The intra-receiver, relative detection times for many of the seismic waveforms observed across our network suggest they emanate from local sources. Therefore, we used our geophone network to locate the larger of these icequakes that registered detections on three or more receivers. To obtain these locations, we computed travel-time delays from an attenuation compensating cross-correlation analysis developed for this study.

In applying this analysis, we first prepared the data from our detection catalog by time reversing and re-processing each waveform with the power detector to compute the signal end-time. The data samples outside the (original) forward and reverse-detected times were then muted (zero-weighted) to eliminate noise exterior to the waveform interval. We next applied a frequency-dependent attenuation model [Futterman, 1962] in an attempt to correct for the individual propagation-path effects from each waveform and improve our estimate of cross-correlation time delays. These path effects were considered to result from attenuation and dispersion in the near-surface ice [Gusmeroli et al, 2010; Jones et al. 2013; Peters et al. 2012], and caused a given icequake's waveforms to appear dissimilar on each geophone. We therefore processed the waveforms using a causal Futterman filter to model the effects of attenuation and dispersion [Pujol, 2003]. This filter has a frequency-domain expression given by:

	$A(\xi) = \exp(-\pi\xi t^*) \cdot \exp\left(-2\pi\xi t^* \ln\left \frac{\xi}{\xi_0}\right \right)$	(1)
--	--	-----

Here, ξ is frequency in Hertz, t^* is an attenuation parameter, and ξ_0 is the digitizer's Nyquist frequency (100Hz). Filters were computed by numerically solving for the value of t^* (seismic wave travel time / seismic quality factor) that maximized the intra-receiver cross-coherency coefficient between each icequake's filtered waveforms. Correlation-derived relative time delays between geophones were then compared with relative delays computed over a homogenous, 2-m resolution source grid. We used a wave speed of $c = 1670 \text{ m sec}^{-1}$ [Mikesell et al., 2012] to compute these times after a visual inspection suggested that the processed data primarily consisted of Rayleigh waveforms. Additionally, we dynamically updated our geophone locations over time to account for ice sheet motion using the co-located GPS receivers. The grid-search point that minimized the absolute sum of these time-delay differences provided an estimate for

each icequake's epicentral solution. Solutions exterior to the network, or with misfits exceeding 0.25 sec, were regarded as too uncertain for reliable interpretation and were discarded. We applied this location method to a limited subset of large icequakes (435 of $\sim 3.4 \cdot 10^4$ total) that were automatically selected based upon high waveform SNR values. Seismic quality factors (Q) were estimated by dividing the source-to-receiver travel time by the inverted value for t^* and averaging the results over the network.

3.3 Seismic Source Size and Waveform Attenuation

To gain additional insight into the mechanism for shallow-ice seismicity, we used relationships between seismic magnitude and source region size to estimate the deformation scale produced at each of the 435 located icequake's hypocenters. We assumed a crack-like seismic source model, based upon the apparent dominance of Rayleigh waveform phases and visual evidence of surface fractures. The volumetric change δV caused by such a seismic source in confined media [pg. 62, Aki and Richards, 2009] is given by:

	$\delta V = \frac{M_0}{\lambda + 2\mu}$	(2)
--	---	-----

where λ and μ denote elastic Lamé parameters, and $\lambda + 2\mu$ is the longitudinal modulus of the ice. δV is approximately related to the moment magnitude M_0 (dyne-cm) through the surface wave magnitude M_S [Mikesell et al., 2012]:

	$\log_{10}(M_0) \cong 1.5 (M_S + 10.7) \text{ where: } M_S = 1.5 \cdot \log_{10}\left(\frac{A}{T}\right) + F(R)$	(3)
--	--	-----

Here, $\frac{A}{T}$ is the maximum Rayleigh wave amplitude-to-period ratio in microns/sec, and $F(R)$ is the amplitude correction for a source-to-receiver distance of R . Volume-change estimates like Equation 2 sometimes include the bulk modulus $\lambda + \frac{2}{3}\mu$ instead [Bowers and Hudson, 1999], which refers to the stress-free volume change of a planar crack. We prefer Equation 1, which gives the ice confined volume change as a combination of the moment required to open a crack and to elastically push the surrounding ice away [Müller, 2001]. This “pushing” creates a

displacement amplitude A_0 at the icequake source ($R = 0$) that is related to the geophone-recorded amplitude $A(R)$ by:

$$A(R) = \left(\frac{A_0}{\sqrt{R}} \right) \exp \left(-\frac{\pi R}{cQT} \right), \quad (4)$$

where Q is the dimensionless surface-wave seismic quality factor, and c and T are wave speed and period, respectively.

To prepare the data for magnitude estimation, we deconvolved the instrument response of the L-28 geophone from the waveforms to obtain displacement records over [2.5, 40] Hz. Initial waveform amplitudes A_0 and attenuation factors π/cQT were then simultaneously inverted using a linear regression of Equation 3, combined with Equation 4. This regression effectively extrapolated measured Rayleigh wave amplitudes to a zero epicentral distance where $F(R) = 0$.

3.4 Relative Magnitude Analyses

To determine if repeatable icequake sources released increasing energy over time, and thereby indicated enhanced ice deformation, we analyzed magnitude changes within icequake multiplets spatially localized to the same region. Such multiplets comprise clusters of variable-magnitude icequakes that reoccur as distinct seismic events, have similar hypocenters, and produce highly correlated seismograms (e.g., Moriya et al. 2003). We identified these events by computing the multi-channel cross-correlation coefficients between waveforms from all 435 located icequakes. This coefficient generalizes the sample-correlation between pairs of single-channel waveforms to pairs of multichannel waveforms, which represent measurements of seismic velocity recorded by a clock-synchronized geophone network [Harris, 1991; Gibbons and Ringdal, 2006]. Such a multichannel signal, sampled at rate Δt , is represented as a data matrix as follows:

$$\mathbf{w}(t) = [\mathbf{w}_1(t), \dots, \mathbf{w}_k(t), \dots, \mathbf{w}_N(t)], \text{ for } t = t_0, t_0 + \Delta t, \dots, t_0 + N\Delta t. \quad (5)$$

In Equation (5), matrix column $\mathbf{w}_k(t)$ is an N -sample seismogram from geophone k , recorded over T -seconds from absolute reference time t_0 so that $\mathbf{w}_k(t_0 + n\Delta t)$ refers to sample n from

geophone k . The correlation coefficient $\rho_{1,2}$ that quantifies the similarity between two different multi-channel signals $\mathbf{w}^{(1)}(t)$ and $\mathbf{w}^{(2)}(t)$, recorded from two different events, is derived from a maximum likelihood estimate [e.g., Harris, 1991], given by:

$$\rho_{1,2} = \max_{\Delta t} \left\{ \frac{\text{tr}(\mathbf{w}^{(1)}(t + \Delta t)^T \mathbf{w}^{(2)}(t))}{\|\mathbf{w}^{(1)}(t)\|_F \|\mathbf{w}^{(2)}(t)\|_F} \right\}, \quad (5)$$

where $\|\bullet\|_F$ is the matrix Frobenius norm and $\text{tr}(\bullet)$ denotes the matrix trace. When only a subset of network geophones were logging data in a given period, just those matrix columns containing operational stations were compared. We thereby required three or more stations to be operational at any time and only included event-pairs where $\rho \geq 0.5$ (subscripts omitted) for analyses. This correlation threshold gave a $\leq 10^{-6}$ false-attribution probability between each event pair, as determined by the correlation-coefficient's empirical null distribution (e.g., [Weichecki-Vergara 2001; Carmichael, 2013]). We then clustered the waveforms of located icequakes into groups based upon this correlation coefficient by using a complete linkage algorithm [Carmichael *et al.* 2012; Allstadt *et al.* 2014]. The relative seismic magnitude ΔM of an event with data matrix $\mathbf{w}^{(2)}(t)$ in a given cluster, compared to a reference event with data matrix $\mathbf{w}^{(1)}(t)$ in that same cluster is then given by [Schaff and Richards, 2014]:

$$\Delta M = \log_{10} \left(\frac{\|\mathbf{w}^{(2)}(t)\|_F}{\|\mathbf{w}^{(1)}(t)\|_F} \right) \quad (6)$$

where the estimator bias due to correlation is removed and the reference event (index 1) is taken to be the earliest within the cluster. Equation (6) provides a more precise means for determining relative magnitudes when compared to methods based on differencing.

3.5 GPS Data Analysis

We processed the GPS data following the general approach of King and Aoki [2003]. First, we analyzed the raw carrier phase and pseudorange GPS data within the GIPSY/OASIS v6.1.2 software using a precise point positioning strategy [Zumberge *et al.*, 1997] by applying uniform

observation weighting and a satellite elevation cutoff angle of 10° . We then estimated station coordinates every 150 sec as a white-noise process, holding the high-rate JPL fiducial satellite orbit and clock values fixed, and estimated white-noise receiver-clock terms and random walk parameters every measurement epoch associated with residual wet tropospheric zenith delays and tropospheric gradients. For the tropospheric mapping function, we adopted the gridded Vienna Mapping Function 1 and computed a priori tropospheric zenith delays from ECMWF grids [Boehm et al., 2006]. At the observation level, we modeled solid Earth tides [Petit and Luzum, 2010] and ocean tide loading displacements using SPOTL [Agnew et al., 1997], as based on the TPXO7.2 ocean tide model [Egbert et al., 2009]. Where possible, we fixed carrier phase ambiguities to integer values [Bertiger et al., 2010]. To minimize day boundary effects, we processed data in 30-hour windows centered on midday and then truncated the time series back to UT days. We then rotated the final coordinate time series into a local North-East-Up coordinate system for further analysis. Remaining outliers, at day boundaries and elsewhere, were visually identified from detrended data and then discarded. Finally, we computed surface velocities in each direction by differentiating positions that were pre-smoothed with a 12-hour width, zero-phase Butterworth filter.

4 Results

We first present general seismic and GPS results without detailed reference to the lake drainage on DOY 169 (Sections 4.1 – 4.5) and describe our cumulative geophysical observations preceding and following this drainage thereafter (Sections 4.6 and 4.7). In section 4.1, we summarize icequake timing, statistics, and temporal variability. In Section 4.2, we identify the dominant seismic Rayleigh phase, and characterize this waveform’s attenuation in the near-surface ice. We then discuss the epicentral distribution, magnitude, and physical dimension of the sources producing these icequakes in Section 4.3. Next, we analyze magnitudes using a quantitative comparison of pre- and post- drainage icequakes in Section 4.4. In Section 4.5, we detail GPS-derived ice surface motion histories, along with spatial-temporal averages of surface speed. Finally, we summarize these geophysical observations to describe the ice-sheet response over time leading up to (Sections 4.6) and following lake drainage (Section 4.7).

4.1 General Icequake Timing and Statistics

Figure 2 shows a subset of the velocity amplitude spectra (spectrograms), computed from the vertical channel of each geophone. These spectrograms revealed several coincident periods of elevated seismicity measured across the network, which are indicated and labeled. We estimated network-averaged dominant frequencies of ~ 15 Hz during these periods, which are somewhat lower than the ~ 25 Hz values reported near our site by others [Jones et al., 2013]. These spectrograms also revealed a strong harmonic signal that is visible starting at about DOY 200 and extending through the remainder of the melt season (not shown). This is somewhat similar to the moulin-resonance signal reported by Roosli et al [2014]. However, an analysis of the resonance modes for the pole used to anchor the seismometer suggests that surface melting caused the geophone-pole platforms to melt out, and induced platform resonance [Carmichael, 2013], which resulted in the harmonic signal. This interpretation is supported by similar observations from a 2009 experiment conducted at the same field site. At this time, similar signals that were coincident with instrument melt out disappeared after site maintenance and fresh installation of the seismometers. Based on these measurements, we truncated our analysis to frequencies ≤ 50 Hz, where energy from seismic waveforms was expected to remain more spatially coherent across the network, and limited our study period from day 165 to 200, when resonance from melt-out was absent or minimal.

Figure 3a illustrates the cumulative number of discrete icequakes detected per hour on three or more geophones, during this study period. This signal shows both long and short period variability in activity. Therefore, to better expose these periods, we computed a spectrogram of the seismicity as well using ~ 1 day long windows with 90% overlap (Figure 3b). This spectrogram of ice quake counts highlighted ~ 10 and ~ 15 day intervals of elevated diurnally variable activity, punctuated by intervals of lower amplitude activity. We evaluated dependencies in this seismicity on time-of-day by binning icequake counts by hour-of-the-day, and excluding times containing drainage-associated events (Figure 3c). The resulting histogram illustrated higher icequake detection rates in early morning hours, with minimum activity occurring near 18:00 local time. The 23:00-hour bin likely underestimated true counts, as seismic data volumes were occasionally truncated before local time 23:30.

Because seismic noise often fluctuates over sub-daily periods in glacial settings [e.g., Walter et al., 2008; Carmichael et al., 2012], we also determined if the diurnal signal and histogram nonuniformity in Figures 3a-c could be produced from variable noise power, rather than by icequake activity. To do so, we estimated the influence of icequake waveform signal-to-noise ratio (SNR) on the performance of our adaptive STA/LTA detector (see Section 3.1). This required computing hourly estimates of four processed noise parameters shaping the detection statistic's F -distribution function. We then used these parameters to compute the threshold SNR required to achieve a 95% detection probability for each hour of each day, as detailed elsewhere [Appendix A.5, Carmichael, 2013]. These threshold SNR values were then averaged into time-of-day bins for comparison with SNR averages computed from detected waveforms, using an unbiased SNR estimator [Kubokawa et al., 1993]. The detected-waveform SNR averages consistently exceeded the respective threshold SNR by several dB (Figure 3d). Thus, we conclude that the diurnal seismicity was produced by geophysical sources, and not caused by changes in noise variance that suppressed or elevated detection rates.

4.2 General Seismic Phase Characteristics

After assembling icequake detections, we identified waveform phases by visually reviewing ~5000 seismic record sections that were randomly drawn from the detection population over the recording period. Common features of these waveforms include ~1-sec signal widths, spectral energy peaks at ~15 Hz (in agreement with mean spectrogram peak energy) and displacement-waveform wavelengths of ~330 m. Waveforms from the same source often appeared dissimilar on distinct vertical geophone channels (Figure 4a, black signals) and only showed substantial coherence after attenuation modeling (Figure 4a, blue signals), thereby indicating that the glacial ice was dissipative over array-aperture scale propagation distances, with a seismic quality factor of $Q \sim 35$ at typical waveform frequencies (Figure 4b). Our analysis also revealed consistent differential time lags present between the horizontal and vertical channels of the largest-amplitude waveform phase (Figures 5a, b). These relative lags are characteristic of Rayleigh waves that originate from shallow or surficial sources [Deichmann et al. 2000, Mikesell et al., 2012, Roosli et al., 2014]. Thus, we conclude that the dominant source of seismicity (95% by number of events) is surficial fracturing. By contrast, only a minority of waveforms (~5%) observed from our sample exhibit characteristics of pure body-wave arrivals. Many from this

minority population are attributable to sources external to the lake region based on their relative arrival times within the geophone network. Consequently, surficial sources produced most of the local seismicity.

4.3 Seismic Source Location and Size Distribution

Figure 6a illustrates the epicentral distribution of the 435 icequakes that we located in the lake basin and its immediate vicinity. Events occurring from the time preceding drainage until 24 hours after drainage (white) dominantly cluster on the upstream side of the lake basin, with a particularly high density of events located near the drainage crack tip, downstream of the moulin (Figure 6b). Events occurring after drainage generally cluster northwest and downstream of these earlier icequakes (blue). While our locations include only a small fraction of all total events (435 of $\sim 10^4$ in number), they represent the largest observed icequakes (highest SNR) and are ostensibly the most significant. We refer to our results for the lake drainage timeline in Sections 4.6-4.7 for additional detail on these location differences.

Figure 7a illustrates the distribution in surface wave magnitudes (mean $M_S \sim 0.41$) for the events located in Figure 6, along with the distribution of seismic quality factors that were computed during magnitude regression (Figure 7b). These quality factors (mean $Q \sim 45$) generally agree with the values that we estimated from the attenuation waveform model and implemented during location (mean $Q \sim 35$), and are additionally consistent with values computed from an alpine Alaskan glacier (e.g., from Mikesell et al. [2012]); this consistency increases our confidence in the location and quality factor estimation methods. Figure 7c shows the corresponding estimates of deformation volume at the seismic source hypocenter (mean $\delta V = +0.85 \text{ m}^3$). Assuming a fracture model, these volumes changes are equivalent in scale to crack-face opening displacements of $\sim 1 \text{ mm}$ over fracture planes of area $\sim 1000 \text{ m}^2$. Such features match field observations of newly formed surface cracks (e.g., Figure 6c) that appeared near site NLBS during early mornings over a 2-3 day period. The remaining, unlocated icequakes likely originated from cracks that were smaller than the sources that triggered the 435 located events shown in Figure 6a, since they produced lower SNR waveforms.

4.4 Relative Icequake Magnitude Analyses

We further analyzed seismic magnitudes of the 435 located events to determine if increased seismicity surrounding the lake drainage event or thereafter also produced larger individual icequakes, and if multiplets produced successively larger icequakes that indicated increased fracture growth. This analysis included assessing changes in magnitude with time duration surrounding the lake drainage event, changes with epicentral distance from the drainage crack, and changes in magnitude for repeating icequakes over reemission time.

To first evaluate temporal changes, we compared the mean surface-wave magnitudes of two different data samples: icequakes occurring within 24 hours of estimated drainage time on DOY 169 versus icequakes occurring ≥ 24 hours before or after drainage time (\bar{m}_{T1} versus \bar{m}_{T2} , Figure 8a). We then used a likelihood ratio test [e.g., Kay, 1998] to determine if these sample sets had similar statistical distributions at a 95% significance level. While we did not censor events by proximity from the crack tip, we did remove outlier influence within this test by implementing a modified sample variance estimator that subtracted the sample median, rather than the mean, from each sample. Our estimates gave statistically similar values of $\bar{m}_{T1} = 0.58$ and $\bar{m}_{T2} = 0.38$, with associated sample standard deviations of 0.47 and 0.53 (in magnitude units). Using these estimates, our likelihood test could not reject the hypothesis that the two sample sets had identical distributions, albeit with only marginal significance ($\sim 96\%$). Therefore, we cannot confidently conclude that individual icequakes before the drainage were significantly larger in magnitude than those occurring after drainage.

We next evaluated any spatial variability in event size by comparing surface-wave magnitudes of icequakes with epicentral solutions ≤ 250 meters from the crack axis to those with epicentral solutions ≥ 250 meters from it (\bar{m}_{D1} versus \bar{m}_{D2}). As before, we tested for distributional similarity between these two populations using a likelihood ratio test after accounting for outlier influence. We again found statistically similar mean magnitudes of $\bar{m}_{D1} = 0.34$ and $\bar{m}_{D2} = 0.38$ between the populations, and respective sample standard deviations of 0.33 and 0.42 (in magnitude units). Therefore, individual icequakes located near the drainage crack were not significantly larger compared to those located remotely from it.

Finally, we assessed any increased growth in fracture size by comparing relative magnitudes of icequakes within multiplets against event separation time. Using Equation 6, we estimated magnitude differences ranging from $\sim 10^{-4}$ (effectively identical events) to ~ 1.5 among 65 distinct clusters that contained between 2 and 13 similar events. Multiplets comprised $\sim 62\%$ of located drainage-associated events, $\sim 40\%$ of located post-drainage events, and $\sim 32\%$ of all available, located events. We examined the significance of any magnitude changes within each of these sample sets by testing relative magnitudes as binomial random variables, since this required the fewest assumptions on the data. Under this hypothesis, we assigned positive relative magnitudes as “successes” and computed their maximum likelihood probabilities and associated uncertainties. We thereby determined $\sim 60\%$ chance that multiplet magnitudes increased over time, among each population, but the uncertainty on this estimate was too large to be evidential. (Figure 8b).

These results collectively indicate that fractures producing icequakes did not significantly change size with time surrounding lake drainage, with distance from the drainage crack, or at multiplet source locations indicating active, repeated fracture growth.

4.5 General GPS Observations

Figure 9 illustrates 12-hour moving-averages of GPS speeds at each network receiver along with the daily-averages in uplift history at site NL08. These time series are color coded according to latitude relative to site FL03, and are truncated between DOY 165-200 to only show data free of filtering end effects, which were also coincident with the seismic records. These speeds maintained above winter values for effectively the whole record, and show periods of inter-station variability that appear temporally coincident with speedup events, as well as some local peaks in uplift. Other portions of these signals appear coherent across the network, with unclear diurnal variability. We therefore examined whether there was detectable diurnal variation in strain across our network by computing temporal averages over intra-station range in speed. Because it is difficult to measure diurnal patterns in GPS that are comparable to anticipated diurnal noise variability [King et al., 2008], we evaluated day-scale changes in strain over the network by assuming that coincident noise variation was common to all receivers. This is reasonable since the GPS antennas were located well above the snow/ice surface, and hence

should be affected by a small multipath signal, the dominant site-specific GPS error. The remaining errors within the diurnal band originated from large-scale geophysical processes or satellite clock and orbit errors, both of which are common to all sites that we selected from our closely spaced GPS network.

Under this assumption, we computed maximum differential speeds between distinct GPS sites and binned them by time of day as follows. We first compared the post-processed speeds for each GPS receiver at every time sample and computed the difference between the maximum and minimum of these measured speeds, over the whole network (i.e., network range in speeds). This produced a time series for the intra-network GPS speed range that we then binned by hour, for each individual day. The speed differences within each bin were then averaged over days to compute a mean, hourly speed range over the relevant observation period; only dates following DOY 169 was used in this binning to avoid biasing the data with hours coincident with drainage-induced speedup.

This calculation proved insensitive to diurnal noise common to each GPS site, since the speed differencing removed the same noise trends. Our estimates therefore provided a variance-reduced computation of the mean, peak speed gradient as it depends on hour of day. Figure 10 shows that these averages are larger during late night/early morning hours, and lowest during mid-day hours. We computed an uncertainty estimate for speed range in each bin using a 4 m a^{-1} standard error for the 12 hr filtered time series, which was further reduced by $1/\sqrt{30}$ through bin averaging over 30 (statistically independent) days. Assuming that the cumulative position error was uniformly distributed among constituent days, these estimates provide a 0.2 cm day^{-1} uncertainty ($\sim 15\%$ of the peak-to-peak difference), indicating that higher late evening/early morning speed gradients relative to mid-day are also physical.

4.6 Geophysical Response Leading up to and Through Lake Drainage

To summarize ice sheet response for times < 24 hours after drainage, we compare the temperature record, icequake timing, epicentral distribution, and GPS history from DOY 165-170. The first notable event shown in our comparison between temperature, GPS speed, uplift and seismicity (Figure 9a-9c) occurs three days prior to lake drainage (June 15th, DOY 166), at

which time elevated icequake activity accompanies uplift and an increase in surface speeds to 0.5 m/day or ~200% the average winter velocity. Epicentral solutions for icequakes located during this time (Figure 6) cluster south of the eventual drainage moulin (purple arrow), proximal to GPS station NL08. Seismic activity subsequently decreases through DOY 168, while uplift ceases and speed remains relatively stable across the network. During this time, the highest air temperatures over the observation period were recorded, and likely produced substantial meltwater input to the lake. These high temperatures were then followed by lake drainage at early local time on June 18th (DOY 169). This drainage coincided with rapid uplift at NL08 (0.6 m), an overall increase in both sliding speeds (~1.0 m/day) and their spatial variability, as well as a peak in icequake activity (up to 220 events/hour); because the exact timing of the initial drainage event is unknown, it is unclear if this peak included any precursory seismicity indicative of the impending hydrofracture. Icequakes leading up to, and within 24 hours after this hydrofracture predominantly clustered immediately west of the drainage moulin and likely indicate relatively high fracture density there. A substantial majority (~62%) of these events were attributed to multiplets and almost certainly represent locations of active, repeated fracture propagation (discussed in Section 4.4).

4.7 Post-Drainage Geophysical Response

The day following drainage (DOY 170, Figures 9a-c) is characterized by a dramatic decrease in seismicity and the return of ice velocities to pre-drainage values, at ~150% of the average winter speed. Associated uplift gradually subsides over the two weeks following drainage, and is punctuated by a brief episode of renewed uplift on DOY 176 that accompanies increased speeds. A subsequent peak in this uplift coincides with a several-day period of increased seismicity that is marked by diurnally variable amplitudes. These amplitudes then decrease to ~50% of their mean value by DOY 183, as uplift completes subsidence. Daily temperatures never drop below 0°C after DOY 185, likely resulting in sustained melt production. Surface speeds show another local maximum near DOY 190, after which time icequake activity remains strongly diurnal, and shares no obvious point-wise correlation with GPS motion. This activity also shows no clear point-wise relation with temperature data, and is occasionally correlated with temperature peaks, while being anti-correlated other times. However, the average hourly seismicity (Figure 10) does exhibit an early morning maximum and mid-day minimum that is anti-correlated with average

timing in peak melt production, and conversely, correlates with the nightly/early morning maximum and mid-day minimum in hourly GPS speed-range. The seismicity also shows a longer-period component of elevated variability that is superimposed on the diurnal signal. This longer-period activity appears to comprise ~15-day patterns in which daily minimum icequake counts remain relatively steady compared with their peak-to-peak amplitudes. By DOY 200, geophone data are unreliable due to resonance of the instrument-platform assembly, likely caused by melt out (see Section 4.2).

Icequakes located over the post-drainage period generally cluster west of those occurring through DOY 169, roughly in the direction of ice flow (Figure 6a, blue markers). These sources are predominantly located farther from the crack, and nearer the zone of extensional strain located in the direction of a subglacial ridge to the northwest (see Figure 1). The region of enhanced seismicity further collocates with increased ice flow on the down-stream side of the lake basin and in the direction of an expected migration path for melt water supplied to the bed by moulins.

5.0 Discussion

Our first and most general result is that seismicity in the lake basin and its immediate vicinity was predominantly (~ 95%) caused by fracture propagation within near-surface ice. These shallow fractures produced Rayleigh waves before and after drainage, indicating that seismogenic deformation was concentrated within a wavelength (~330 m) of the ice surface. Average surface-wave magnitudes of icequakes that we located ($M_S \sim 0.41$; Figure 7) are more than a half a magnitude unit greater than those measured from Rayleigh waves triggered by surface cracking on an alpine glacier [Mikesell et al. 2012]. From a crack-source model, we estimate that these events produced average volume changes of $\sim 1\text{m}^3$ per icequake, equivalent to crack-face opening displacements of ~ 1 mm over fracture planes of area $\sim 1000\text{ m}^2$. Such dimensions are consistent with thin (mm-width) cracks extending over tens of meters that we observed during and immediately after lake drainage (Figure 6c).

This result is somewhat contrary to our initial assumptions. We expected post-drainage seismicity to dominantly involve basal seismicity once sliding, and ostensibly basal deformation, increased. Instead, body waveforms indicative of deeper icequakes comprised only ~5% of the

icequake population at any time. Further, seismicity was most active at night when speed gradients peaked on average (Figure 10), but absolute speeds (and basal sliding) were at near minimum.

5.1 Discussion: Lake Drainage

Supraglacial lake drainage coincides with a transient increase in surficial seismicity characterized by ~100 icequakes per hour with magnitudes that are statistically similar to those occurring more than a day before or after drainage. If precursory seismicity accompanies supraglacial lake drainage, it may occur over time scales that are too short to be clearly discriminated from the seismicity directly caused by hydrofracture or uplift. The relative absence of associated basal seismicity during drainage suggests a lack of rapid seismogenesis at the ice-bed interface during enhanced sliding. Such aseismic deformation could indicate the presence of a plastic till layer, or that drainage-facilitated ice deformation is not sufficiently elastic to seismically radiate within our geophone's pass band. A qualitatively similar dominance of surficial seismicity has also been observed from an alpine glacier during speedup triggered by a proglacial lake drainage [Roux *et al.*, 2010], and from a polythermal glacier with bed over-deepening [Pomeroy, *et al.*, 2013], where sliding is known to occur. These results support a model in which transient melt-triggered sliding influences seismicity primarily by promoting high rate surface strains that cause ice fracture.

While lake drainage greatly influenced emission rates of icequakes, it did not seem to detectably influence the relative size of individual icequake magnitudes. This suggests that seismic source size is not heavily controlled by transient uplift or speedup events coincident with drainage, and that icequakes can relieve elevated ice column stresses rapidly enough so that associated stress build up does not trigger larger, less frequent icequakes. If magnitude changes do exist, they are too small relative to the variability of the absolute magnitudes to be easily observed. In this case, larger epicentral sample sizes are necessary to provide definitive conclusions. We suggest that detecting such differences requires an increased emphasis on assembling large datasets of icequake locations so that estimator variance of relative magnitudes is further reduced.

5.2 Discussion: Post Drainage

Diurnally variable icequake activity persists throughout most of the post-lake drainage record, despite changes in background seismicity (Figures 3a - 3b). It is most pronounced during the early morning hours and cannot be explained from fluctuations in background noise that reduce icequake detections (Figure 3c-3d). These intervals of elevated activity are concurrent with low surface temperatures and meltwater production and may reflect associated cycles in mechanical or thermal influence on ice deformation, as discussed below. Heightened activity during these hours is also consistent with field observations, in which audible cracking was heard near the NLBS site (Figure 1) and newly formed surface cracks were observed during early mornings over a 2-3 day period (Figure 6c). One source of surficial seismicity producing these signals may be local fluctuations in surface strain that induce the surface cracking. Decreased meltwater input to the bed during early mornings may increase spatial variability in basal traction as lubricating meltwater declines so that patches of the bed and overlying ice come into contact. This could induce associated spatial variations in surface strain, at length scales shorter than resolvable with our GPS network (~ 2 ice thicknesses), that leads to seismogenic cracking.

A link between surface seismicity and basal water input is also consistent with the shift in icequake locations shown in Figure 6a. Prior to drainage, it was likely that the bed received most local water input from the active southwest moulin indicated in Figure 6b. After drainage, the water input through the lake moulin would have increased total water delivery to the region where seismic activity then increased. The addition of this moulin north of the southwest moulin coincides with the northward shift of the mean pre-drainage and post-drainage epicentral points that are respectfully shown by the white and blue markers in Figure 6a. This would suggest that spatial differences in input location, and therefore basal lubrication, drive the high seismogenic strains.

Figure 10 gives additional support for the presence of a feedback between surface strain and seismicity. It illustrates the point-wise range in GPS speeds measured across the network, averaged into hour-of-day bins. Here, maximum flow differences (on average) peak with increases in average icequake activity during early morning hours. If this timing were unrelated to diurnal modulation (e.g., melt input), we would expect no significant hourly differences in peak speed gradients. Additionally, if this diurnal modulation is related to diurnal variability in

meltwater input as we have proposed, then decreased melt input drives the measured spatial flow differences. This is again consistent with a model in which increases in spatially variable basal traction induce surface strains that open seismogenic tensile cracks.

Finally, it is also possible that thermal effects may trigger some or all of the seismogenic surface fracturing. Prior observations elsewhere suggest that when strong temperature gradients cause elastic contraction in the shallow subsurface, they can induce tensile fracturing [C. Thurber, personal communication, 2012; Bradley, 1948]. Alternatively, meltwater produced during warm hours in mid-day may refreeze at night within the cold sub-surface in a process similar to the freeze-thaw cycles that break water-occupied porous rocks through heaving [Murton et al., 2006]. Such experiments have demonstrated that pressures can greatly exceed the tensile strength of ice [Dash et al., 2006]. Therefore, it seems plausible that thermal effects may trigger fracture propagation in the ice. We emphasize that these thermal effects may also act in parallel with spatial strain gradients to explain our observations.

5.3 Comparison with Regional Flow Patterns

The above-nominal winter values in surface speed (Figure 9b) indicate that surface ice may have been undergoing extensional flow during our observation period. Our local GPS network, however, does not provide a good representation of the large-scale spatial variation in speed. We therefore compare our seismic locations with TerraSAR-X data for 2009 and 2010, which provide 11-day average estimates of the spatial variation in speed [Joughin et al., 2013], as we lack corresponding data from 2011. The data show substantial spatial variation in speed from one 11-day period to the next and presumably average out greater day-to-day variation. Although these maps of flow enhancement are from different years than the seismic data, they do reveal similar spatiotemporal patterns in the two years prior to seismic measurement, indicating similar variability is likely to have occurred in 2011. In fact, our epicentral estimates co-locate with the two regions of relatively high ice speed in 2009 and 2010 (Figure 11), where extensional strain was likely high due to the comparatively slow upstream ice, and favorable for tensile fracturing that produces icequakes. Furthermore, the data indicate the potential for relatively rapid (days) km-scale transitions between tensile and compressive strain rates. Thus, summer speed

enhancement may transiently produce regions of tensile strain within the lake basin where strains are compressive throughout the winter.

In addition, our seismic data show ~10-15 day periods in elevated activity that is likely indicative of enhanced surface fracture that is punctuated by relative low amplitude variability. These changes are also consistent with the temporal complexity documented by Joughin et al. [2013] in proximity to the same moulins shown in Figure 11. This TerraSAR-X imagery shows fluctuations of nearly 100% in surface speeds relative to winter values using ~10-day averaged surface velocities. Our seismicity shares this variability, and indicates associated speed variations may also occur over shorter periods. Although we had difficulty resolving such change in the GPS data, such variation may be occurring at length scales shorter than can be resolved with our GPS-network ($< \sim 2$ km, or 2 ice thicknesses). Alternatively, the TerraSAR-X image data provides comparatively high-spatial resolution velocity maps of Greenland's ablation zone and may provide a more useful supplement to seismic array observations over comparative sensing apertures.

Conclusions

In this work, we used a network of geophones and GPS instruments to monitor ice-sheet response before, during, and after the drainage of a km-scale supraglacial lake in Greenland's ablation zone. We developed and implemented statistically robust detection methods that provided high-confidence estimates of icequake activity, location, seismic attenuation and magnitudes for comparison with GPS-measurements of displacement and speed. We demonstrate that seismic networks provide evidence for melt-season surface fracturing at a fine spatial resolution, and a relative deficiency in deeper, brittle deformation within the ice column.

Cumulatively, our observations indicate that the post drainage spatial and temporal relationship between GPS speeds, temperature, and seismicity is complex in the lake-forming region. While icequake epicenters generally shift northwest from drainage-associated locations once a new moulin opened, subsequent seismicity shows an unclear relationship with time histories of GPS-derived speeds and uplift. Icequake magnitudes also show no significant change with drainage-crack proximity or timing of drainage. Seismicity did, however, show heightened activity during

early morning hours when the average range in GPS-speeds peaked (Figure 10) and absolute speeds are at minimum. There also is spatial coincidence with regions of repeatable, high surface speeds measured during previous years (Figure 11) when data were available. This suggests that localized spatial variations in ice deformation, rather than sliding speed, may provide a better predictor for elevated seismic activity. Since surface speeds were almost uniformly above mean winter values network-wide before drainage (Figure 9b), the ice may have undergone significant extensional (tensile) strain at that time, despite flow into the lake basin being generally more compressive. This evidence therefore suggests that icequakes triggered by tensile fracturing may reflect stress modulations relative to an enhanced tensile stress state that differs from the value predicted by average flow characteristics. Further, our data requires this model of ice sheet flow to be modulated by a corresponding diurnal forcing mechanism like meltwater input. Thermal effects may also act in concert with this melt-forcing modulation to produce the observed diurnal variability in seismicity.

Our results indicate that the physical mechanisms controlling transient ice-sheet response are still not well understood on scales spanning several ice thicknesses. Further, the lack of detectable basal seismicity with and without enhanced sliding suggests either that instruments with a lower-frequency pass-band are required to detect such motion, or that seismogenic stick-slip motion may not take place at ice-bed interface in lake forming region due to enhanced creep or till deformation.

Acknowledgements

The authors would like to thank Matt Hoffman for constructive discussions on GPS processing and subglacial hydraulics, Brooke Medley for input regarding exposition, David Shean for photographic data of instrument melt out, and James Pitton for input on detection statistics. Research by J. Carmichael was supported by a NASA NESSF Fellowship Grant NNX08AU82H and NSF Grant ANT-0424589. The fieldwork and additional analyses were supported by the National Science Foundation's Office of Polar Programs (NSF-OPP) through ARC-1023382, awarded to I. Joughin and ARC-1023364, awarded to S. B. Das and M. D. Behn. Matt King is a recipient of an Australian Research Council Future Fellowship (project number FT110100207).

References

- Allstadt, K., and S. D. Malone (2014), Swarms of repeating stick-slip icequakes triggered by snow loading at Mount Rainier volcano, *J. Geophys. Res. Earth Surf.*, 119, 1180–1203, doi:10.1002/2014JF003086.
- Agnew, D. C. (1997), NLOADF: A program for computing ocean-tide loading, *J. Geophys. Res.*, 102(B3), 5109–5110.
- Anandakrishnan, S. and R. Alley (1997), Tidal forcing of basal seismicity of ice stream C, West Antarctica, observed far inland, *Journal of Geophysical Research-Solid Earth*, 102(B7), 15183–15196, doi: 10.1029/97JB01073.
- Bartholomew, I., P. Nienow, A. Sole, D. Mair, T. Cowton, S. Palmer, and J. Wadham (2011), Supraglacial forcing of subglacial drainage in the ablation zone of the Greenland ice sheet, *Geophys. Res. Lett.*, 38, L08502, doi: 10.1029/2011GL047063.
- Blandford, R. R., (1974), An Automatic Event Detector At The Tonto Forest Seismic Observatory, *Geophysics*, 39(5), 633–643.
- Boehm, J., B. Werl, and H. Schuh (2006), Troposphere mapping functions for GPS and very long baseline interferometry from European Centre for Medium-Range Weather Forecasts operational analysis data, *J. Geophys. Res.*, 111, B02406, doi:10.1029/2005JB003629.
- Bertiger, W., S. Desai, B. Haines, N. Harvey, A. Moore, S. Owen, and J. Weiss (2010), Single receiver phase ambiguity resolution with GPS data, *J. Geodesy*, 84(5), 327–337, doi: 10.1007/s00190-010-0371-9
- Boon, S. and M. Sharp (2003), The role of hydrologically-driven ice fracture in drainage system evolution on an Arctic glacier, *Geophys. Res. Lett.*, 30(18), 1916, doi: 10.1029/2003GL018034.
- Box, J. E. and K. Ski (2007), Remote sounding of Greenland supraglacial melt lakes: implications for subglacial hydraulics, *J. Glaciol.*, 53(181), 257–265, doi: 10.3189/172756507782202883.
- Bradely, Charles C. (1948), Mendota Quake, *American Journal of Science*, 246(6) 390, doi:10.2475/ajs.246.6.390
- Canassy, P. D., J. Faillietaz, F. Walter, and M. Huss (2012), Seismic activity and surface motion of a steep temperate glacier: a study on Triftgletscher, Switzerland, *J. Glaciol.*, 58(209), 513–528, doi: 10.3189/2012JoG11J104.
- Carmichael, J. D., E. C. Pettit, M. Hoffman, A. Fountain, and B. Hallet (2012), Seismic multiplet response triggered by melt at Blood Falls, Taylor Glacier, Antarctica, *J. Geophys. Res. -Earth Surf.*, 117, F03004, doi: 10.1029/2011JF002221.

731 Carmichael, Joshua D. *Melt-Triggered Seismic Response in Hydraulically-Active Polar Ice:*
732 *Observations and Methods*. PhD thesis, University of Washington, 2013, uri:
733 <http://hdl.handle.net/1773/25007>

734 Chen, X., P. M. Shearer, F. Walter, and H. A. Fricker (2011), Seventeen Antarctic seismic events
735 detected by global surface waves and a possible link to calving events from satellite images,
736 *Journal of Geophysical Research-Solid Earth*, 116, B06311, doi: 10.1029/2011JB008262.

737 Cuffey, K. and W. S. B. Paterson (2011), *The Physics of Glaciers*, Elsevier, Butterworth-
738 Heinemann, Amsterdam [u.a.].

739 Danesi, S., S. Bannister, and A. Morelli (2007), Repeating earthquakes from rupture of an
740 asperity under an Antarctic outlet glacier, *Earth Planet. Sci. Lett.*, 253(1-2), 151-158, doi:
741 10.1016/j.epsl.2006.10.023.

742 Das, S. B., I. Joughin, M. D. Behn, I. M. Howat, M. A. King, D. Lizarralde, and M. P. Bhatia
743 (2008), Fracture propagation to the base of the Greenland Ice Sheet during supraglacial lake
744 drainage, *Science*, 320(5877), 778-781, doi: 10.1126/science.1153360.

745 Das, Sarah B., Behn, Mark D, and Joughin (2011), Modes of Supraglacial Lake Drainage and
746 Dynamic Ice Sheet Response. In American Geophysical Union, Fall Meeting 2011.

747 Dash, J. G., A. W. Rempel, and J. S. Wettlaufer (2006), The physics of premelted ice and its
748 geophysical consequences, *Reviews of Modern Physics*, 78(3), 695-741, doi:
749 10.1103/RevModPhys.78.695.

750 Davidson, G. and J. Nye (1985), A Photoelastic Study of Ice Pressure in Rock Cracks, *Cold Reg.*
751 *Sci. Technol.*, 11(2), 141-153, doi: 10.1016/0165-232X(85)90013-8.

752 Doyle, S. H., A. L. Hubbard, C. F. Dow, G. A. Jones, A. Fitzpatrick, A. Gusmeroli, B. Kulesa,
753 K. Lindback, R. Pettersson, and J. E. Box (2013), Ice tectonic deformation during the rapid in
754 situ drainage of a supraglacial lake on the Greenland Ice Sheet, *Cryosphere*, 7(1), 129-140, doi:
755 10.5194/tc-7-129-2013.

756 Egbert, G. D., S. Y. Erofeeva, S. C. Han, S. B. Luthcke, and R. D. Ray (2009), Assimilation of
757 GRACE tide solutions into a numerical hydrodynamic inverse model, *Geophys. Res. Lett.*, 36,
758 doi:10.1029/2009gl040376.

759
760 Futterman, W. I. (1962), Dispersive Body Waves, *Journal of Geophysical Research*, 67(13),
761 5279-&, doi: 10.1029/JZ067i013p05279.

762 Gibbons, S. J. and F. Ringdal (2006), The detection of low magnitude seismic events using
763 array-based waveform correlation, *Geophysical Journal International*, 165(1), 149-166, doi:
764 10.1111/j.1365-246X.2006.02865.x.

765 Gusmeroli, A., R. A. Clark, T. Murray, A. D. Booth, B. Kulesa, and B. E. Barrett (2010),
 766 Seismic wave attenuation in the uppermost glacier ice of Storglaciaren, Sweden, *J. Glaciol.*,
 767 56(196), 249-256.

768 Harper, J. T., J. H. Bradford, N. F. Humphrey, and T. W. Meierbachtol (2010), Vertical
 769 extension of the subglacial drainage system into basal crevasses, *Nature*, 467(7315), 579-582,
 770 doi: 10.1038/nature09398.

771 Harris, D. B., Lawrence Livermore National Laboratory, United States. Dept. of Energy, and
 772 United States. Dept. of Energy. Office of Scientific and Technical Information. (2006), Subspace
 773 Detectors Theory.

774 Hoffman, M. J., G. A. Catania, T. A. Neumann, L. C. Andrews, and J. A. Rumrill (2011), Links
 775 between acceleration, melting, and supraglacial lake drainage of the western Greenland Ice
 776 Sheet, *J. Geophys. Res. -Earth Surf.*, 116, F04035, doi: 10.1029/2010JF001934.

777 Howat, I. M., S. de la Pena, J. H. van Angelen, J. T. M. Lenaerts, and M. R. van den Broeke
 778 (2013), "Expansion of meltwater lakes on the Greenland Ice Sheet", *Cryosphere*, 7(1), 201-204,
 779 doi: 10.5194/tc-7-201-2013.

780 Johansson, A. M., P. Jansson, and I. A. Brown (2013), Spatial and temporal variations in lakes
 781 on the Greenland Ice Sheet, *Journal of Hydrology*, 476, 314-320, doi:
 782 10.1016/j.jhydrol.2012.10.045.

783 Jones, G. A., B. Kulesa, S. H. Doyle, C. F. Dow, and A. Hubbard (2013), An automated
 784 approach to the location of icequakes using seismic waveform amplitudes, *AoG Annals of*
 785 *Glaciology*, 54(64), 1-9.

786 Joughin, I., B. E. Smith, I. M. Howat, D. Floricioiu, R. B. Alley, M. Truffer, and M. Fahnestock
 787 (2012), Seasonal to decadal scale variations in the surface velocity of Jakobshavn Isbrae,
 788 Greenland: Observation and model-based analysis, *J. Geophys. Res. -Earth Surf.*, 117, F02030,
 789 doi: 10.1029/2011JF002110.

790 Joughin, I., S. B. Das, M. A. King, B. E. Smith, I. M. Howat, and T. Moon (2008), Seasonal
 791 speedup along the western flank of the Greenland Ice Sheet, *Science*, 320(5877), 781-783, doi:
 792 10.1126/science.1153288.

793 Kamb, B. (1987), Glacier Surge Mechanism Based on Linked Cavity Configuration of the Basal
 794 Water Conduit System, *Journal of Geophysical Research-Solid Earth and Planets*, 92(B9),
 795 9083-9100, doi: 10.1029/JB092iB09p09083.

796 Kay, S. M., (1998), *Fundamentals of Statistical Signal Processing: Volume II*, Prentice-Hall
 797 PTR, Englewood Cliffs, N.J.

798 King, M., and S. Aoki (2003), Tidal observations on floating ice using a single GPS receiver,
 799 *Geophys. Res. Lett.*, 30(3), 1138, doi:10.1029/2002GL016182.

800 Leeson, A. A., A. Shepherd, S. Palmer, A. Sundal, and X. Fettweis (2012), Simulating the
801 growth of supraglacial lakes at the western margin of the Greenland ice sheet, *Cryosphere*, 6(5),
802 1077-1086, doi: 10.5194/tc-6-1077-2012.

803 Moriya, Hirokazu, Hiroaki Niitsuma, and Roy Baria. "Multiplet-clustering analysis reveals
804 structural details within the seismic cloud at the Soultz geothermal field, France." *Bulletin of the*
805 *Seismological Society of America* 93.4 (2003): 1606-1620, doi: 10.1785/0120020072

806 Mikesell, T. D., K. van Wijk, M. M. Haney, J. H. Bradford, H. P. Marshall, and J. T. Harper
807 (2012), Monitoring glacier surface seismicity in time and space using Rayleigh waves, *J.*
808 *Geophys. Res. -Earth Surf.*, 117, F02020, doi: 10.1029/2011JF002259.

809 Murton, J. B., R. Peterson, and J. Ozouf (2006), Bedrock fracture by ice segregation in cold
810 regions, *Science*, 314(5802), 1127-1129, doi: 10.1126/science.1132127.

811 Palmer, S., A. Shepherd, P. Nienow, and I. Joughin (2011), Seasonal speedup of the Greenland
812 Ice Sheet linked to routing of surface water, *Earth Planet. Sci. Lett.*, 302(3-4), 423-428, doi:
813 10.1016/j.epsl.2010.12.037.

814 Peters, L. E., S. Anandakrishnan, R. B. Alley, and D. E. Voigt (2012), Seismic attenuation in
815 glacial ice: A proxy for englacial temperature, *Journal of Geophysical Research: Earth Surface*,
816 117(F2), - F02008, doi: 10.1029/2011JF002201.

817 Petit, G., and B. Luzum (2010), IERS Conventions Rep. ISBN 3-89888-989-6, 179 pp, Frankfurt
818 am Main.
819

820 Pomeroy, J., A. Brisbourne, J. Evans, and D. Graham (2013), The search for seismic signatures
821 of movement at the glacier bed in a polythermal valley glacier, *Annals of Glaciology*, 54(64),
822 149-156, doi: 10.3189/2013AoG64A203.

823 Qamar, A. (1988), Calving Icebergs - a Source of Low-Frequency Seismic Signals from
824 Columbia Glacier, Alaska, *Journal of Geophysical Research-Solid Earth and Planets*, 93(B6),
825 6615-6623, doi: 10.1029/JB093iB06p06615.

826 Roux, P., F. Walter, P. Riesen, S. Sugiyama, and M. Funk (2010), Observation of surface seismic
827 activity changes of an Alpine glacier during a glacier-dammed lake outburst, *Journal of*
828 *Geophysical Research-Earth Surface*, 115, F03014, doi: 10.1029/2009JF001535.

829 Schaff, D. P. and P. G. Richards (2014), Improvements in magnitude precision, using the
830 statistics of relative amplitudes measured by cross correlation, *Geophysical Journal*
831 *International*, 197(1), 335-350, doi: 10.1093/gji/ggt433.

832 Schoof, C. (2010), Ice-sheet acceleration driven by melt supply variability, *Nature*, 468(7325),
833 803-806, doi: 10.1038/nature09618.

834 Selmes, N., T. Murray, and T. D. James (2011), Fast draining lakes on the Greenland Ice Sheet,
835 *Geophys. Res. Lett.*, *38*, L15501, doi: 10.1029/2011GL047872.

836 Shepherd, A., A. Hubbard, P. Nienow, M. King, M. McMillan, and I. Joughin (2009), Greenland
837 ice sheet motion coupled with daily melting in late summer, *Geophys. Res. Lett.*, *36*, L01501,
838 doi: 10.1029/2008GL035758.

839 Sitts, D. J., A. G. Fountain, and M. J. Hoffman (2010), Twentieth Century Glacier Change on
840 Mount Adams, Washington, USA, *Northwest Sci.*, *84*(4), 378-385, doi: 10.3955/046.084.0407.

841 Stuart, G., T. Murray, A. Brisbourne, P. Styles, and S. Toon (2005), Seismic emissions from a
842 surging glacier: Bakaninbreen, Svalbard, *Annals of Glaciology*, *Vol 42*, 2005, *42*, 151-157, doi:
843 10.3189/172756405781812538.

844 Sundal, A. V., A. Shepherd, P. Nienow, E. Hanna, S. Palmer, and P. Huybrechts (2009),
845 Evolution of supra-glacial lakes across the Greenland Ice Sheet, *Remote Sens. Environ.*, *113*(10),
846 2164-2171, doi: 10.1016/j.rse.2009.05.018.

847 Tedesco, M., M. Luthje, K. Steffen, N. Steiner, X. Fettweis, I. Willis, N. Bayou, and A. Banwell
848 (2012), Measurement and modeling of ablation of the bottom of supraglacial lakes in western
849 Greenland, *Geophys. Res. Lett.*, *39*, L02502, doi: 10.1029/2011GL049882.

850 M. Tedesco, I.C. Willis, M.J. Hoffman, A.F. Banwell, P. Alexander, and N.S. Arnold.
851 Ice Dynamic Response to two Modes of Surface lake Drainage on the Greenland Ice Sheet.
852 Environmental Research Letters, 8:034007 (9 pp.), Sept. 2013.

853 Thelen, W. A., K. Allstadt, S. De Angelis, S. D. Malone, S. C. Moran, and J. Vidale (2013),
854 Shallow repeating seismic events under an alpine glacier at Mount Rainier, Washington, USA, *J.*
855 *Glaciol.*, *59*(214), 345-356, doi: 10.3189/2013JoG12J111.

856 van der Veen, C. (1998), Fracture mechanics approach to penetration of surface crevasses on
857 glaciers, *Cold Reg. Sci. Technol.*, *27*(1), 31-47, doi: 10.1016/S0165-232X(97)00022-0.

858 Walter, F., J. F. Clinton, N. Deichmann, D. S. Dreger, S. E. Minson, and M. Funk (2009),
859 Moment Tensor Inversions of Icequakes on Gornergletscher, Switzerland, *Bulletin of the*
860 *Seismological Society of America*, *99*(2A), 852-870, doi: 10.1785/0120080110.

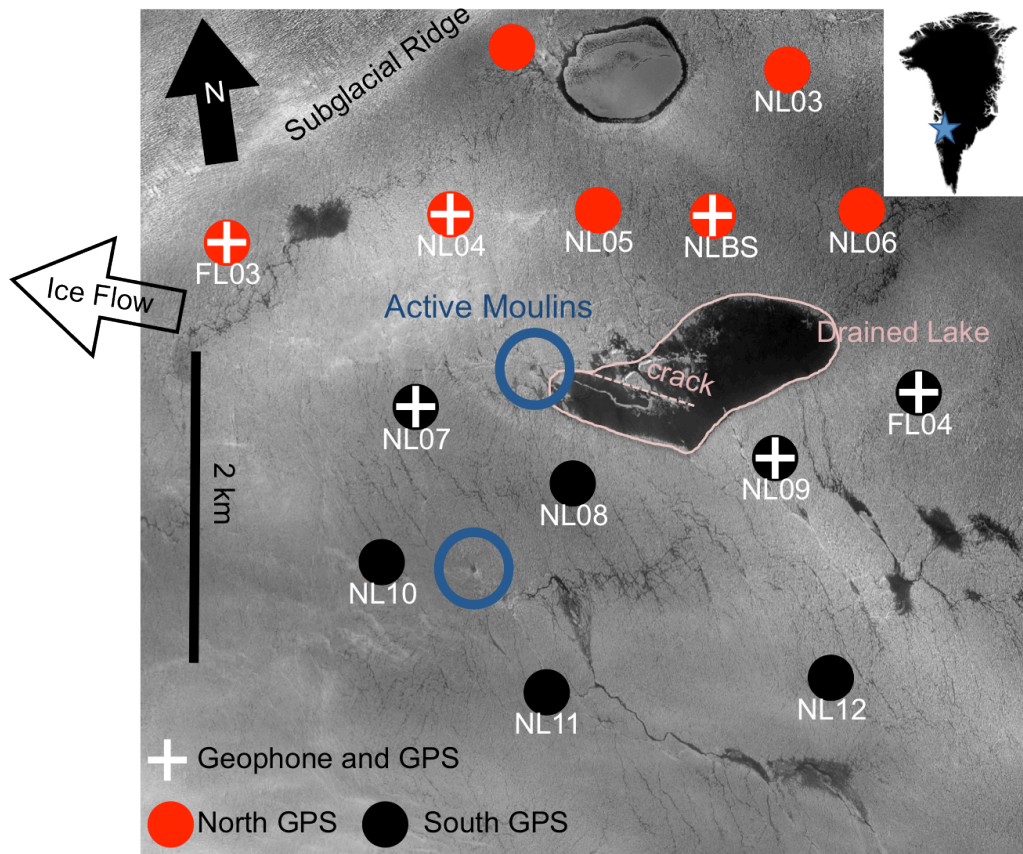
861 Walter, F., N. Deichmann, and M. Funk (2008), Basal icequakes during changing subglacial
862 water pressures beneath Gornergletscher, Switzerland, *J. Glaciol.*, *54*(186), 511-521, doi:
863 10.3189/002214308785837110.

864 Weichecki-Vergara, S., H. L. Gray, and W. A. Woodward (2001), Statistical development in
865 support of CTBT monitoring, Tech. Rep. DTRA-TR-00-22, Southern Methodist Univ., Dallas,
866 Tex

867 Zumberge, J. F., M. B. Heflin, D. C. Jefferson, M. M. Watkins, and F. H. Webb (1997), Precise
868 point positioning for the efficient and robust analysis of GPS data from large networks, J.
869 Geophys. Res., 102(B3), 5005-5017.
870

871

872



873

874

875 **Figure 1.** WorldView image from DOY 168 showing the field site location (68.73°N , 49.53°W)
 876 in a region where supraglacial lakes form in Greenland's ablation zone. The outlined central
 877 dark region in the image center indicates the filled supraglacial lake shortly before drainage
 878 along with an older drainage crack. GPS sites where Trimble GPS receivers were deployed in
 879 June 2011 are shown by filled circles. Crosses show locations of the six L-28, 4.5Hz geophones
 880 that were paired with the GPS stations. Red and black markers respectfully indicate sites North
 881 and South of FL03. Blue circles show the moulin that formed following the lake drainage and a
 882 second nearby moulin that appears to have been active prior to the lake drainage.

883

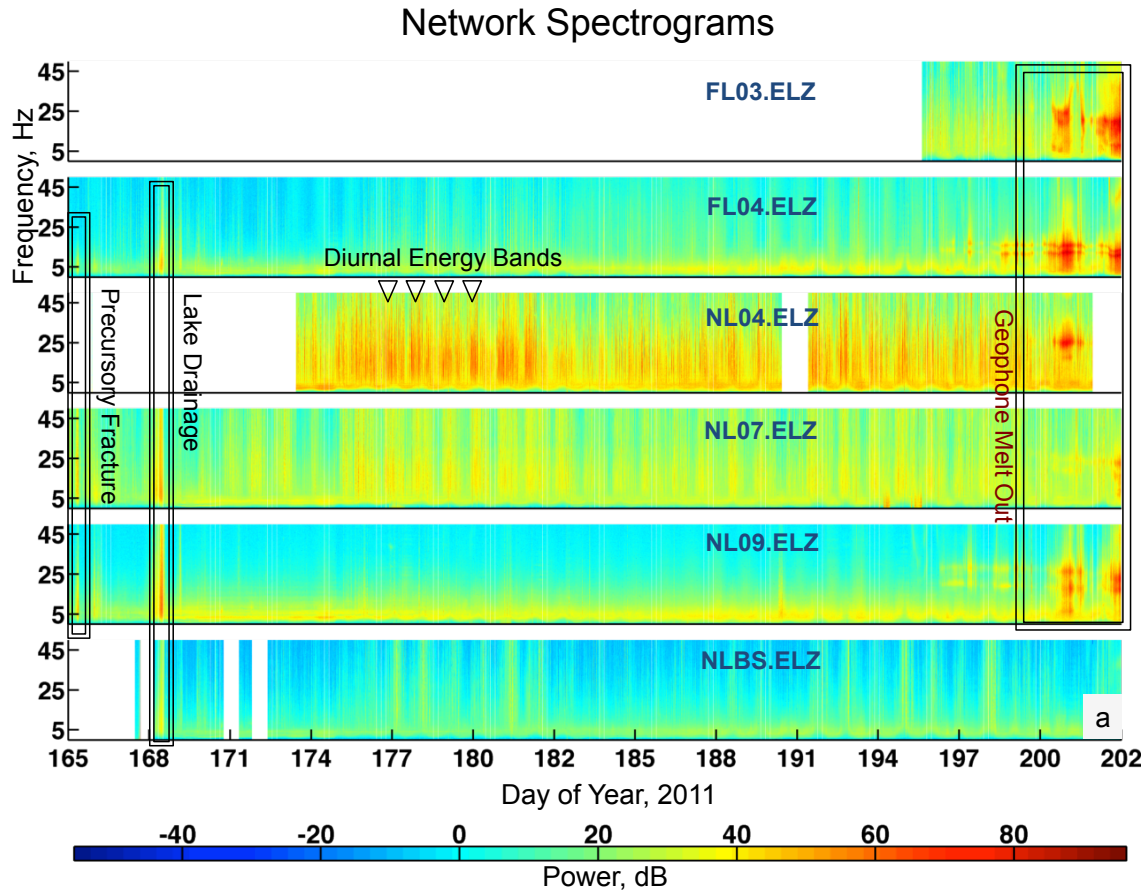


Figure 2 Band-limited spectrograms computed using the vertical component of available geophone data. The color bar indicates the range of signal power in decibels (dB). White regions indicate where only a geophone partial network was logging data. Features documented on this plot include: elevated seismicity preceding hydrofracture, seismicity coincident with lake drainage, diurnal bands of elevated energy, and spectral curves indicating resonance caused by instrument melt out. All data refer to local time.

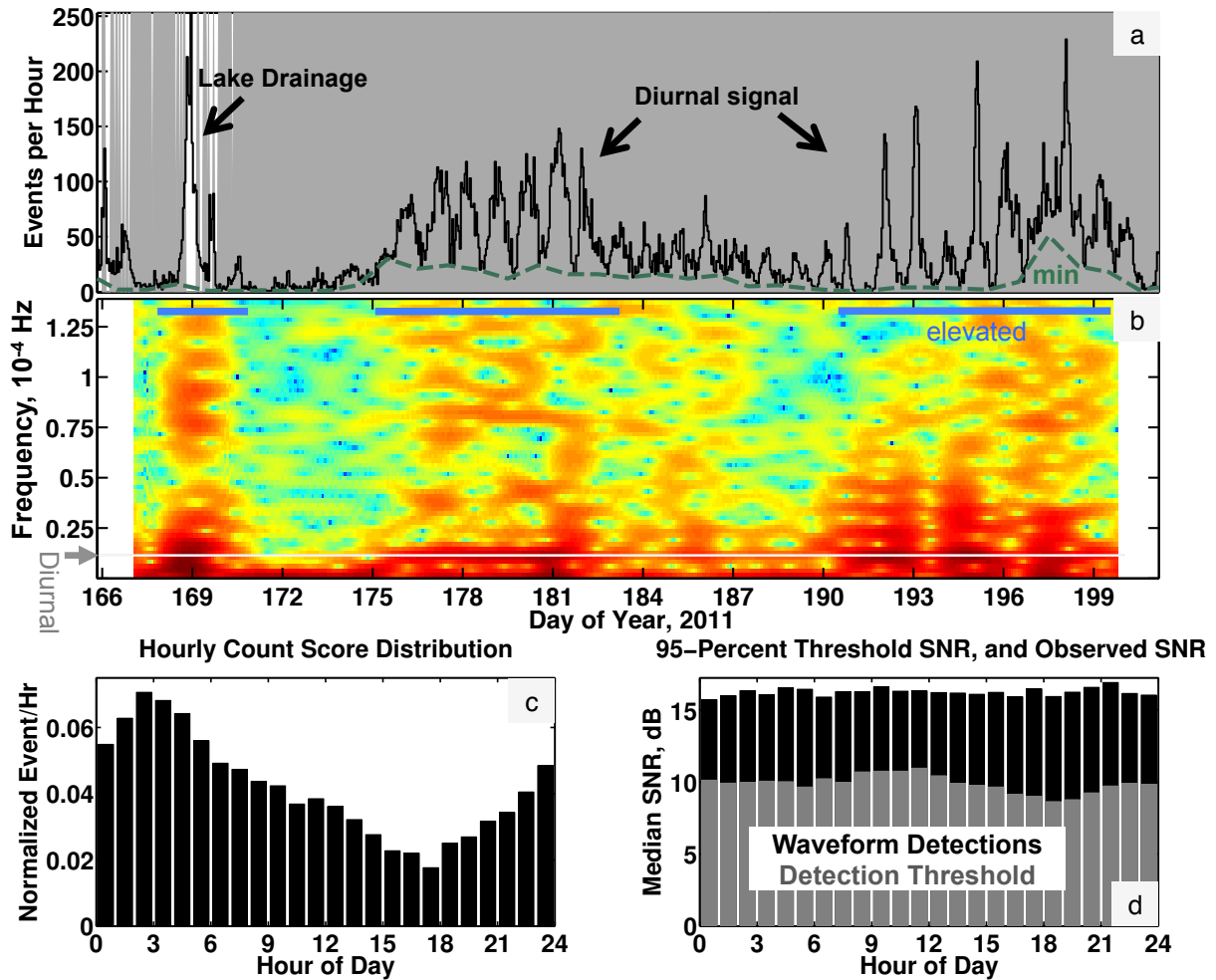


Figure 3 Summary of icequake seismicity and corresponding detection statistics. All dates indicate local time. **(a)** Number of icequakes detected per hour (seismicity) on any 3 or more operational geophones within the network. Peaks prior to and during drainage are labeled for reference, and the green dashed line labeled *min* indicates the minimal count rate in a day. The gray shading indicates bins where the STA/LTA detector statistic's predicted null distribution fit the observed distribution with less than 20% error. **(b)** The spectrogram of the seismicity in (a) with the minimal daily count rate removed. The thin, gray horizontal line indicates the diurnal frequency component, and the blue bars labeled *elevated* indicate intervals of increased short-period variability. Blank portions of the spectrogram end-points are due to spectral windowing. **(c)** Seismicity from (a) binned by hour of day. Days preceding and during drainage were removed from counting. **(d)** Median signal-to-noise ratios (SNR) computed from detected

906 icequake waveforms (black) compared with the median, unbiased SNR thresholds required to
907 achieve a 95% detection probability in each hour. This threshold SNR was conditional upon
908 several noise statistics estimated within each detection window.
909

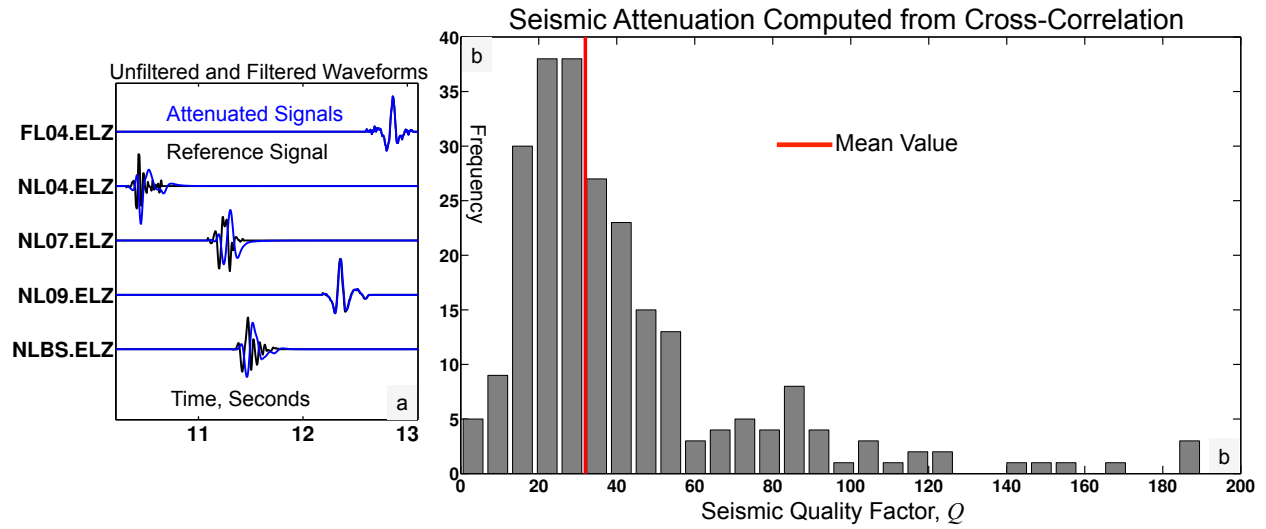


Figure 4 (a) Pre- and post-processed vertical-velocity geophone waveforms used to locate icequakes. Original, recorded waveforms are shown in black. Blue waveforms are causally attenuated to maximally correlate with the latest arriving signal. In this case, the signal measured at FL04 comprised the last arrival and was consequently not processed with the attenuation filter. **(b)** Seismic quality factors (Q) estimated from inverted values of the attenuation parameter t^* that were obtained by maximizing cross-correlation coefficients between waveforms as show in (a). Nonphysical estimates were discarded. These values are in general agreement with attenuation factors computed for two mountain glaciers [Gusmeroli *et al*, 2010; Mikesell *et al.*, 2012] and the estimates obtained independently in Figure 7b.

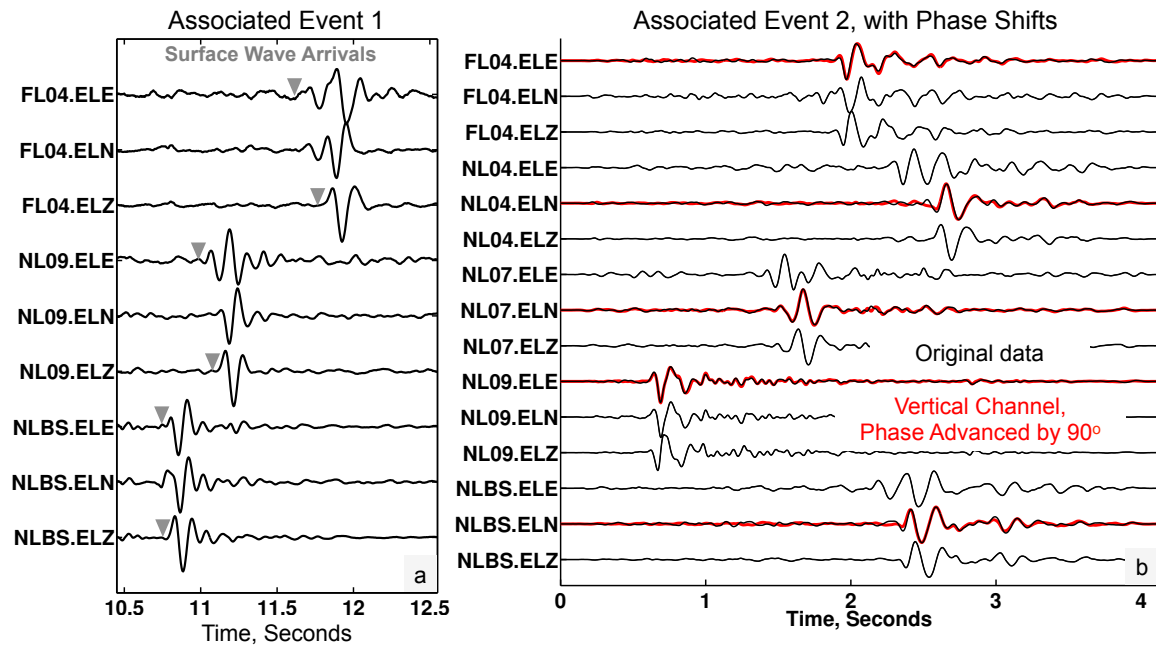


Figure 5 (a) A multi-channel record section illustrating waveforms recorded on 3 of the available 6 geophones for a typical icequake. The gray markers indicate the differential time lags between the vertical and horizontal component of the dominant waveform phase. **(b)** A record section for a second event illustrating comparisons between the vertical and horizontal components of motion. Selected horizontal channels for each geophone are superimposed with 90° phase-advanced (Hilbert transformed) vertical components to illustrate their strong linear correlation (shown in red). The phase-similarity between the horizontal and phase-advanced vertical components is indicative of a Rayleigh wave.

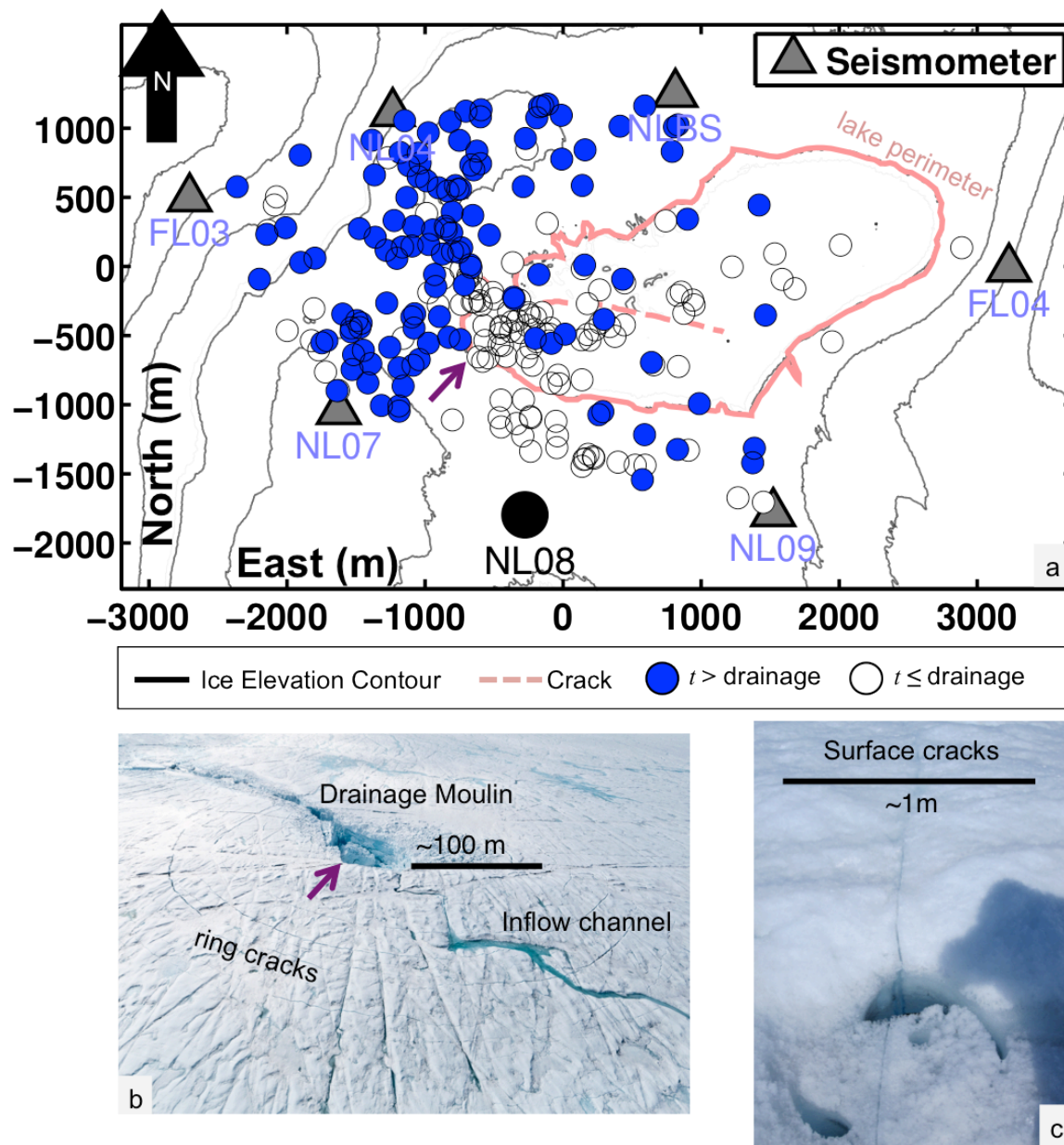


Figure 6 Summary of the icequake locations. **(a)** Epicenters of 435 icequakes plotted over a surface elevation contour map. These were selected from $\sim 3 \cdot 10^4$ total icequakes by requiring events to have pick times from at least 3 geophones and high enough SNR at all stations for reliable waveform identification and thus locating. Events detected before and up to 24 hours after drainage are shown in white. Events detected later are shown in blue. The purple arrow refers to the drainage moulin shown in (b). The local coordinate system origin coincides with the geophone network center. **(b)** The lake-drainage moulin viewed from air. Labeled features

944 include circularly symmetric “ring cracks” that likely developed from tension induced by the ice-
945 void of the moulin, and a meltwater inflow channel. The purple arrow matches that in (a). **(c)**
946 Surface fractures that formed overnight near the NLBS field site during field missions, extending
947 horizontally for tens or hundreds of meters. These cracks produced audible reports and ice
948 motion that was observed by field team members.
949

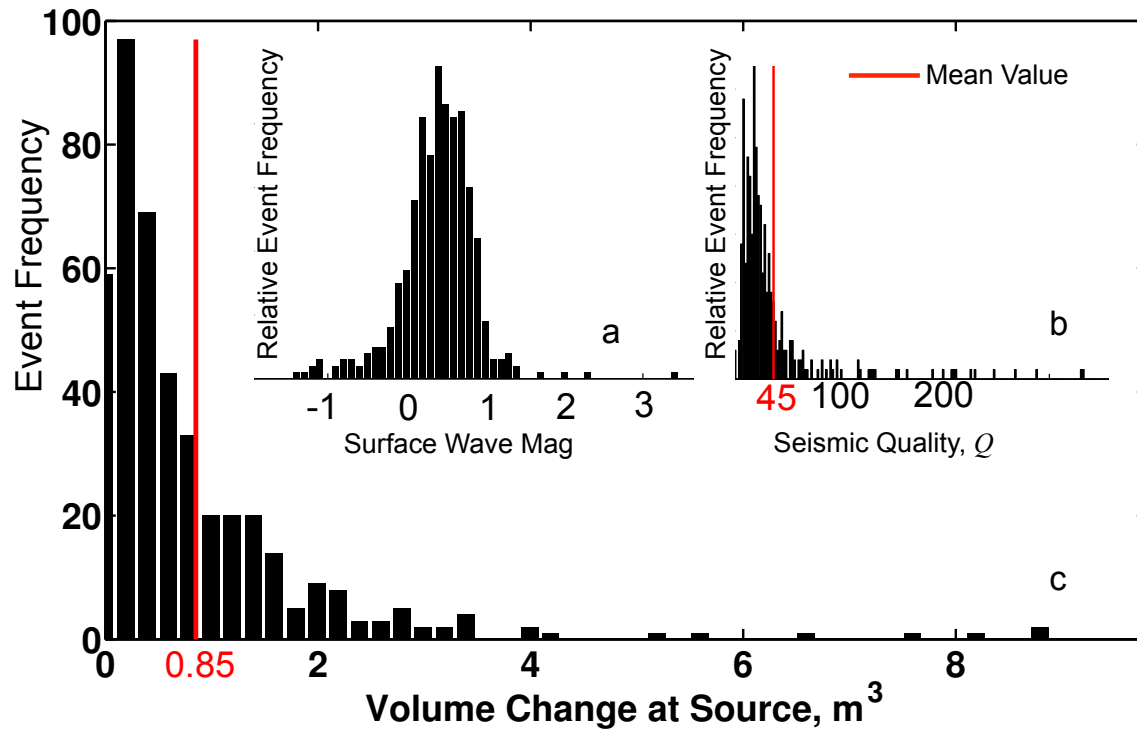


Figure 7 Histograms estimated from located icequake waveform amplitudes and epicentral solutions, with red vertical lines denoting mean values. **(a)** The distribution of surface-wave magnitudes, computed from Rayleigh wave peak amplitudes and period. **(b)** The Rayleigh wave seismic quality factor (Q). Values are within range of those reported in glacial ice elsewhere [e.g., *Mikesell et al.*, 2012] and are consistent with the attenuation factors estimated through correlation (see Figure 5b). **(c)** The distribution for volumetric source growth, using a tensile fracture model. Values were determined by empirical relationships between surface wave and moment magnitudes scales. The cumulative growth in crack space from the 435 icequakes located here is $\sim 360 \text{ m}^3$.

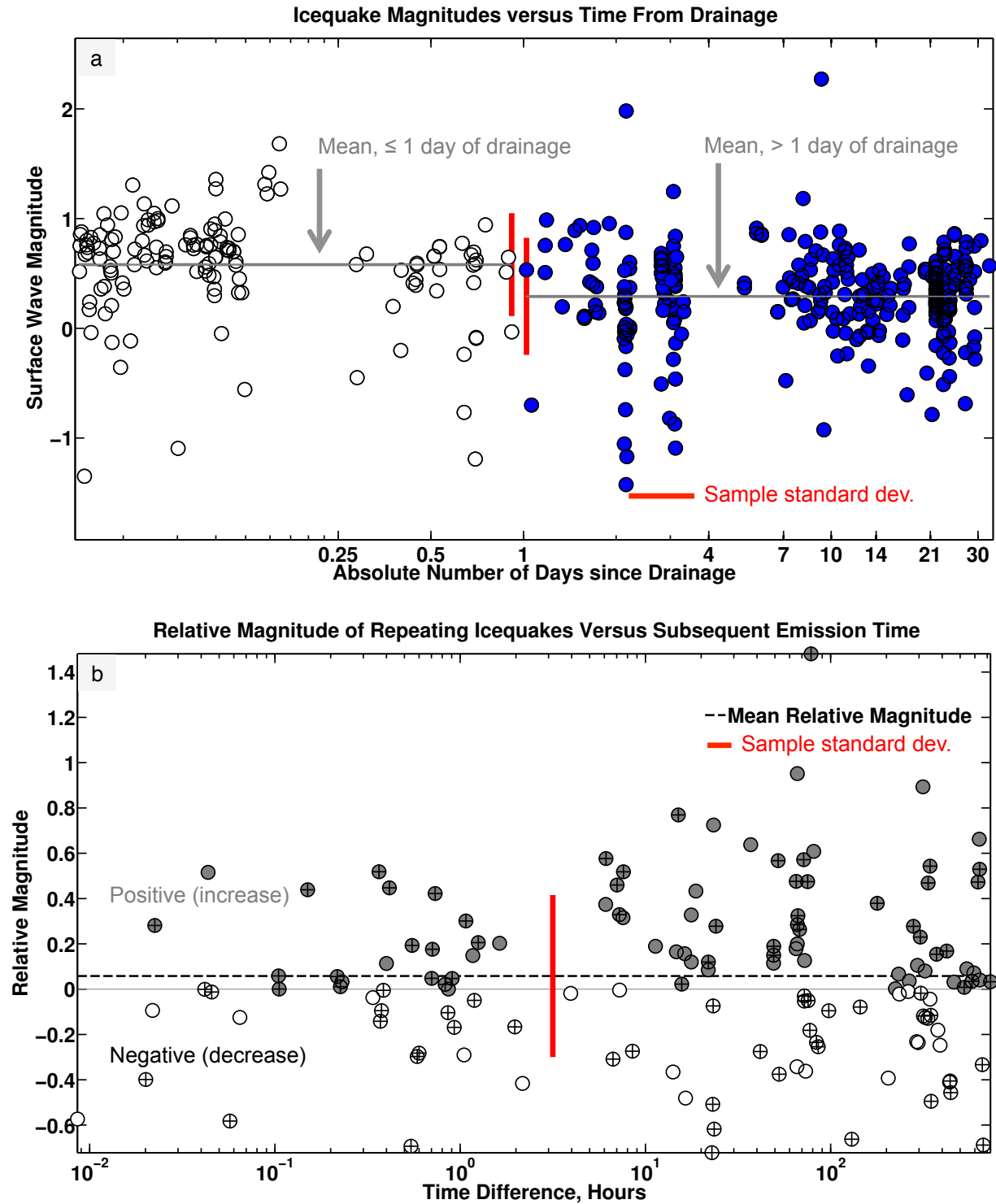
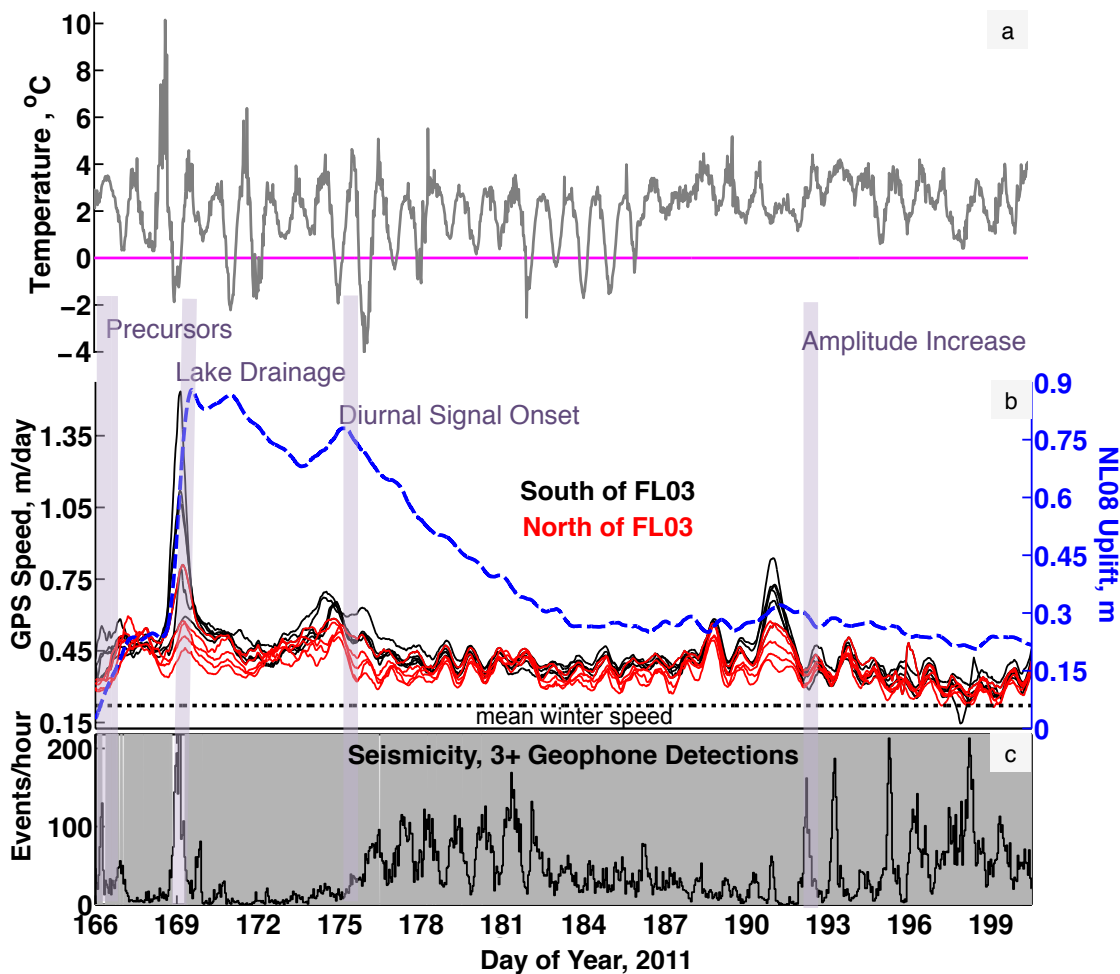


Figure 8 Comparisons between magnitudes of located events versus time since lake drainage and relative magnitudes of repeating icequakes (multiplets) versus time. **(a)** Icequake magnitudes versus time duration from drainage. The left, horizontal gray line shows the sample mean for

surface magnitudes (white markers) occurring within 1 day of drainage. The right gray line shows the respective sample mean of surface wave magnitudes (blue markers) occurring more than a day before or after drainage. The red vertical bars illustrate the respective standard deviations for each sample and indicate statistically similar values between two event populations. **(b)** Relative magnitudes ΔM of icequakes (Equation 6) versus time for repeating events with similar hypocenters and waveforms, each with respect to an initial, reference event. Gray and white markers respectively indicate positive versus negative magnitude changes. The crossed markers indicate magnitudes measured relative to a reference waveform that occurred within 24 hours of lake drainage. There is no statistically significant change in event size versus emission time that would indicate steadily increasing/decreasing source sizes.



979

980

981 **Figure 9** (a) Recorded temperatures measured ~1 m above the ice surface, at the lakeshore. (b)
 982 Relative GPS elevation (blue) measured at site NL08 and ice speeds measured at sites with same
 983 temporal coverage as the geophones (Figure 2). Colors correspond to Figure 1 and indicate sites
 984 North (red) or South (black) of FL03, and the dashed, horizontal line indicates the average winter
 985 speed. (c) Icequake seismicity from Figure 3a; the vertical axis was truncated below the signal
 986 peak to increase the readability of the remaining record. Seismicity and temperature in (a) are
 987 generally anti-correlated, though phase lags vary. Purple bars across each plot indicate events
 988 interpreted from seismicity.

989

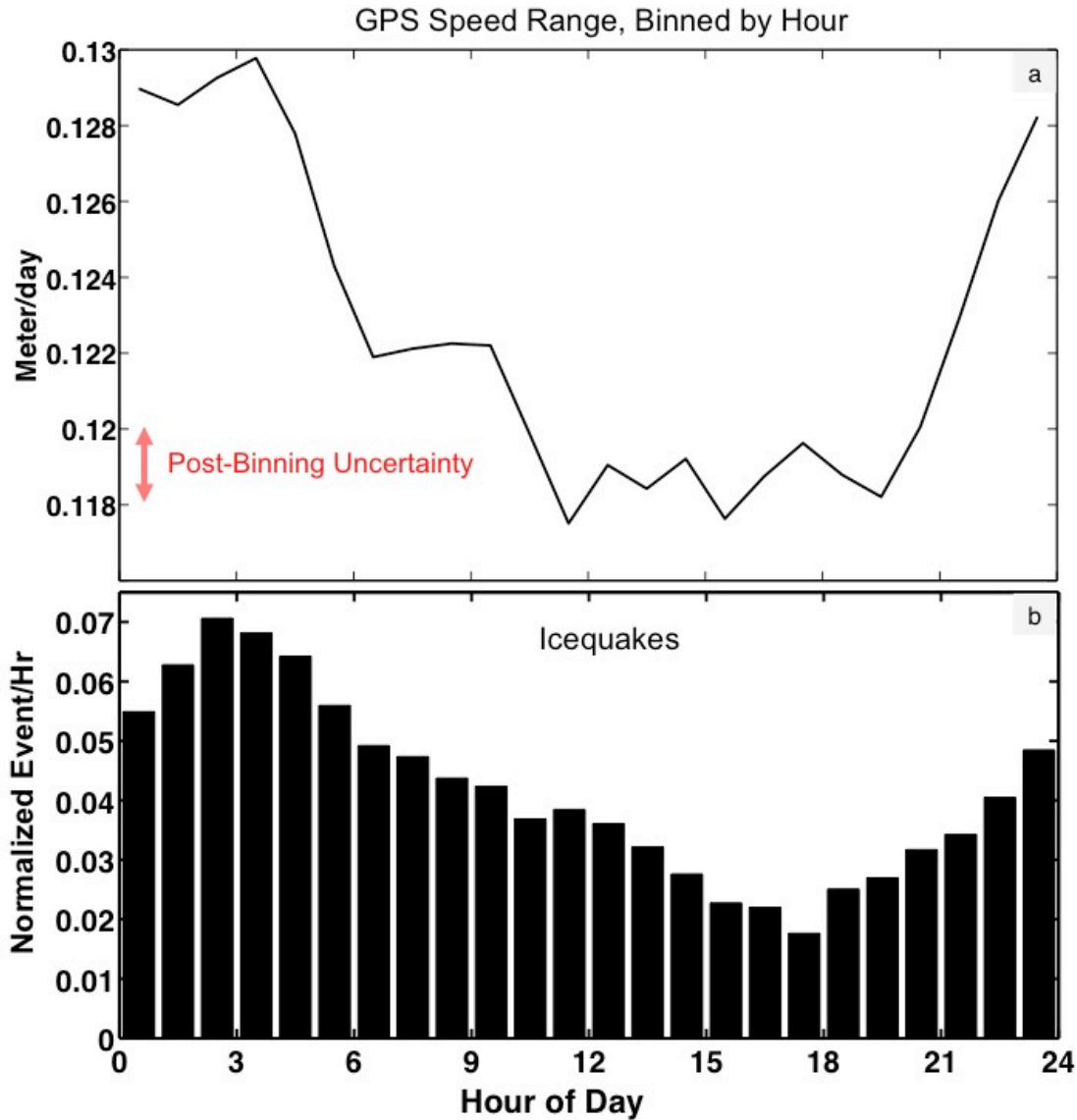


Figure 10 A comparison between the range in GPS speeds and icequake seismicity, binned by hour. **(a)** Differences between the maximum and minimum GPS speeds (range) measured across the network, and averaged by hour. Relative extremum indicate that network-wide spatial variability in speed was higher (on average) during early morning hours, and lower during the day. Uncertainty after variance reduction from hourly binning is $\pm 2 \text{ mm day}^{-1}$. **(b)** The hourly seismicity from Figure 3b, shown for comparison. Data concurrent with the drainage are excluded from counts in each case.

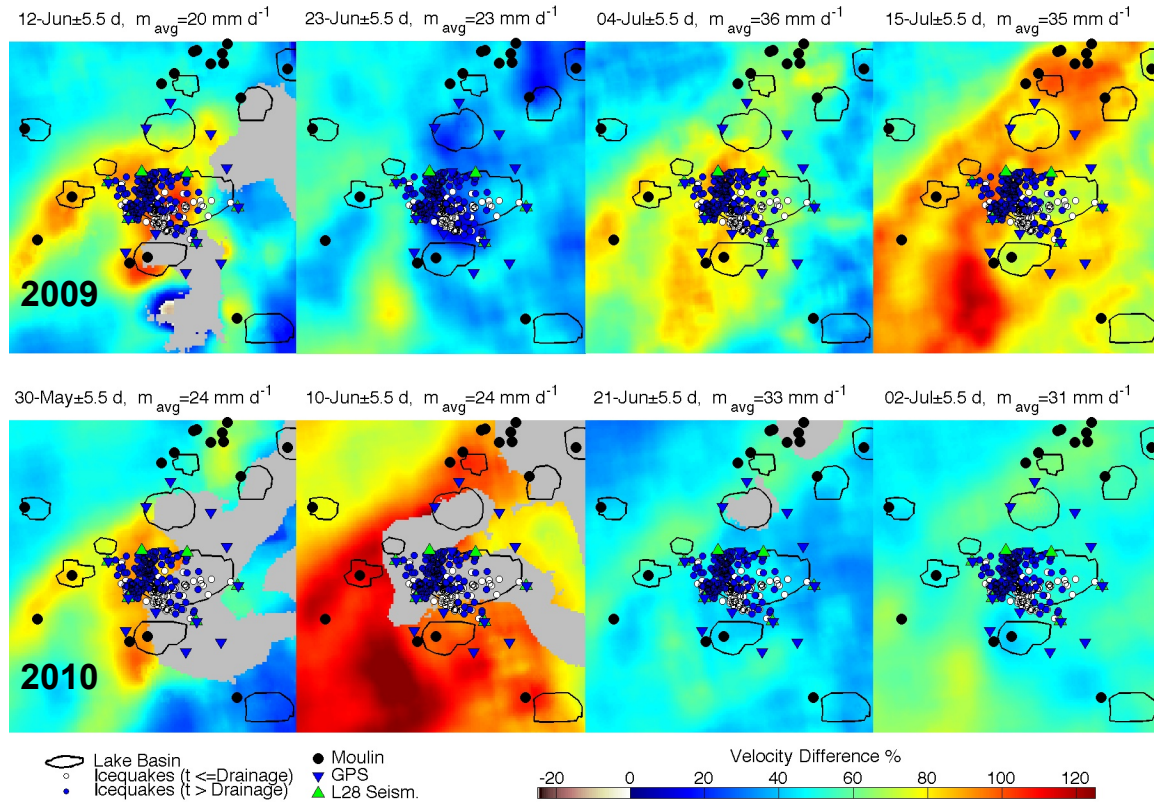


Figure 11 A comparison between velocity mosaics from Joughin *et al* [2013] constructed using TerraSAR-X imagery from 2009 and 2010, superimposed with icequake epicenters from 2011; corresponding data from 2011 were unavailable. The left-most panels illustrate a consistent pattern of enhanced velocity between the two years. Icequakes from Figure 6a are clustered densely along the regions of enhanced velocity present in the previous two years.